Lim *et al. Energy Mater.* **2025**, *5*, 500131
DOI: 10.20517/energymater.2025.63

Energy Materials

Review

Open Access

Rational engineering of hydroxyapatites for sustainable chemicals, H_2, biofuels and CO_2 conversion

Kang Hui Lim[1,#], Ming Hui Wai[1,#], Keyu Cao[1], Sonali Das[2], Ange Nzihou[3,4,5], Sibudjing Kawi[1,*]

[1]Department of Chemical and Biomolecular Engineering, National University of Singapore, Singapore P.O. Box 117585, Singapore.
[2]Department of Chemical Engineering, Indian Institute of Technology Bombay, Powai 400076, India.
[3]Centre RAPSODEE, UMR CNRS 5302, IMT Mines Albi, Universite de Toulouse, Campus Jarlard, Albi F-81013, France.
[4]School of Engineering and Applied Science, Princeton University, Princeton, NJ 08544, USA.
[5]Andlinger Center for Energy and the Environment, Princeton University, Princeton, NJ 08544, USA.
[#]Authors contributed equally.

***Correspondence to:** Prof. Sibudjing Kawi, Department of Chemical and Biomolecular Engineering, National University of Singapore, 1 Engineering Drive 3, Singapore P.O. Box 117585, Singapore. E-mail: chekawis@nus.edu.sg

How to cite this article: Lim, K. H.; Wai, M. H.; Cao, K.; Das, S.; Nzihou, A.; Kawi, S. Rational engineering of hydroxyapatites for sustainable chemicals, H_2, biofuels and CO_2 conversion. *Energy Mater.* **2025**, *5*, 500131. https://dx.doi.org/10.20517/energymater.2025.63

Received: 31 Mar 2025 **First Decision:** 7 May 2025 **Revised:** 14 May 2025 **Accepted:** 27 May 2025 **Published:** 26 Jun 2025

Academic Editor: Yuhui Chen **Copy Editor:** Fangling Lan **Production Editor:** Fangling Lan

Abstract

Chemical and fuel production through conventional catalytic processes requires significant improvement to reduce CO_2 emission levels. Sustainable, potentially direct, chemical production is in critical need, such as methane coupling to olefins, propane dehydrogenation to propylene, biodiesel production, and greenhouse gas emissions modulating reactions, including CO_2-utilizing dry reforming of methane, partial oxidative of methane, CO oxidation, CO_2 methanation are some of the emerging technologies to address sustainability challenges. These technologies remained constrained due to the lack of stable and efficient catalysts. Hydroxyapatite (HAP), a highly functional versatile material, offers great potential due to its flexible tunability, and several studies have outlined the synthesis protocol of HAP and design modifications for catalytic applications. However, a comprehensive understanding of connecting reaction-specific demands to tailor HAP catalyst designs is limited. In this review, we bridge that gap, highlight key challenges in catalytic reactions, and propose the necessary HAP catalyst modifications, including acid-base tuning, defects-induced lattice oxygen or vacancies, mesoporosity modulation, and catalyst active metal species dispersion, to improve catalytic performance by limiting catalyst deactivation from absorbates surface poisoning, sintering, and coking. Finally, future research areas for improvement for HAP catalysts are suggested to advance the maturity of catalytic technologies.

Keywords: Catalysis, dry reforming, CO_2 utilization, renewable energy, cation substitution, anion substitution

INTRODUCTION

Attenuating CO_2 concentration is crucial for mitigating climate change, the key challenge of the 21st century. Creating sustainable, long-term, and economically viable methods for CO_2 capture and valorization is crucial, with heterogeneous catalysts becoming increasingly vital to contemporary sustainable energy strategies[1]. The application of heterogeneous catalysts enables fine chemical and energy production to occur more sustainably. The development of heterogeneous catalysts requires an intimate and fundamental understanding of the catalyst surface at the nano-scale to drive desired catalytic reactions selectively and actively with stable performance. A significant amount of literature has been dedicated to materials for heterogeneous catalysts such as carbons[2,3], metal-organic framework (MOF)[4-6], and metal oxides[3,7,8]. Other than these classes of catalyst support, hydroxyapatite (HAP)-based catalysts have received increasing research attention in the past few decades, as evidenced by an increasing number of publications in Figure 1A.

HAP is a bio-compatible material that constitutes the main mineral component in bone and teeth and is responsible for hardness and strength. This bio-compatible material stirs great interest in many fields due to its remarkable structure and inherent properties. The surface of HAP material contains both acidic and basic elements such as P and Ca, respectively[9]. HAP has often been used as a catalyst or catalyst support for liquid-phase organic reactions, namely, the Suzuki reaction, alcohol oxidation and furfural amination reactions[10,11]. Surface engineering strategies, based on a rational understanding of HAP material properties, are required to unlock the potential of HAP materials for enhanced catalytic performance, product selectivity, and catalytic stability. This is particularly important when HAP materials are to be used as heterogeneous catalysts. Ibrahim *et al.* had written a comprehensive review on the usage of HAP for air and water pollution control[12]. Kaneda and Mizugaki comprehensively covered HAP as a heterogeneous catalyst for organic synthesis reactions and pointed out the possibility of using HAP to solve environmental and energy issues[13]. The synthesis route of HAP material for liquid phase reaction has been critically covered by Fihri *et al.*[14] Sadat-Shojai *et al.* covered HAP synthesis using various methods for different morphologies at length[15]. Recently, a comprehensive textbook on the use of HAP as a catalyst has been covered by Pham Minh *et al.* The improvements in catalytic performance and product selectivity in using HAP catalysts have motivated further research and development to better understand and tune their catalytic properties for the following catalytic reactions for sustainable fuel and chemical production[16]. To conduct a holistic understanding of the role of HAP-based catalysts, we first introduce the advantages and gaps of HAP in sustainable chemicals processes (i.e., oxidative CH_4 coupling to higher order hydrocarbons (OCM), oxidative propane dehydrogenation to propylene (PDH), and biodiesel production), hydrogen production processes (i.e., dry reforming of methane (DRM), partial oxidation of methane (POM), and water gas shift (WGS), CO oxidation coupled with H_2 fuel cell), and CO_2 utilization processes (i.e., CO_2 hydrogenation to CO or CH_4). A fundamental understanding of the HAP material will be subsequently discussed. Subsequently, a focused review of the various surface engineering strategies for HAP-based catalysts and consequential surface effects will be presented [Figure 1B]. A research perspective and outlook for the various surface engineering strategies will be discussed at the end of these sections.

FUNDAMENTAL UNDERSTANDING OF HAP FRAMEWORK

HAP structure

HAP has a hexagonal (P63/m space group) crystal cell with lattice parameters a = 9.37 Å and c = 6.88 Å[17]. In the HAP crystal structure, two distinct types of calcium (Ca) atoms occupy different positions within the unit cell [Figure 2A][18]. Consequently, the chemical formula is expressed as $Ca_{(I)}Ca_{(II)6}(PO_4)_6(OH)_2$. The HAP framework is composed of a dense network of PO_4 tetrahedra, with each PO_4 group contributing to a

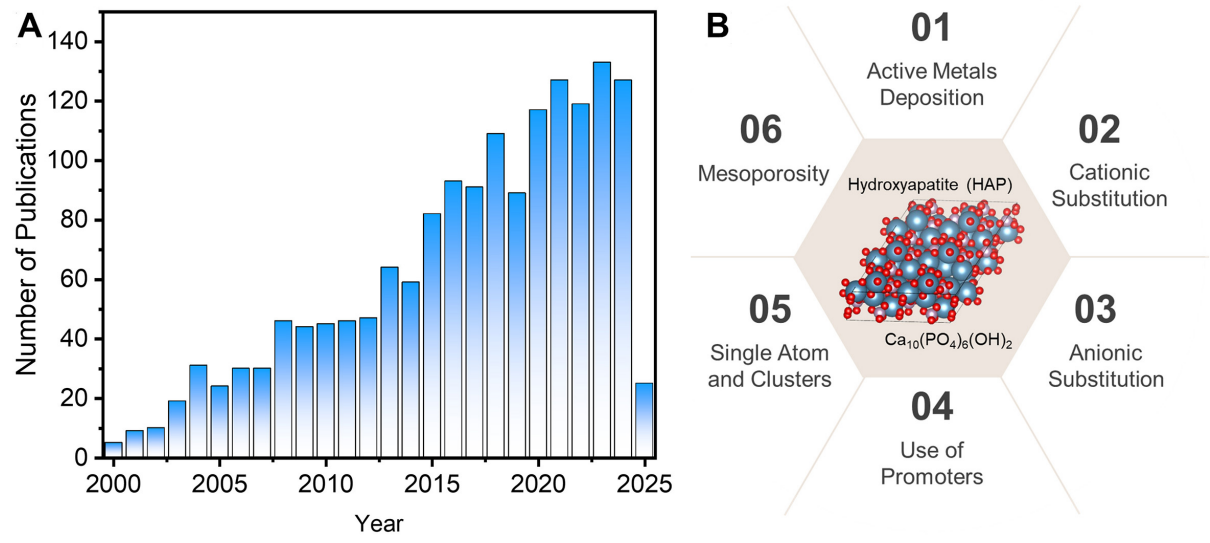

Figure 1. (A) Number of publications using keywords "hydroxyapatite" and "catalyst" from the year 2000 to the year 2025 from Web of Science as of 28 March 2025. (B) Schematic of the various surface engineering strategies for HAP.

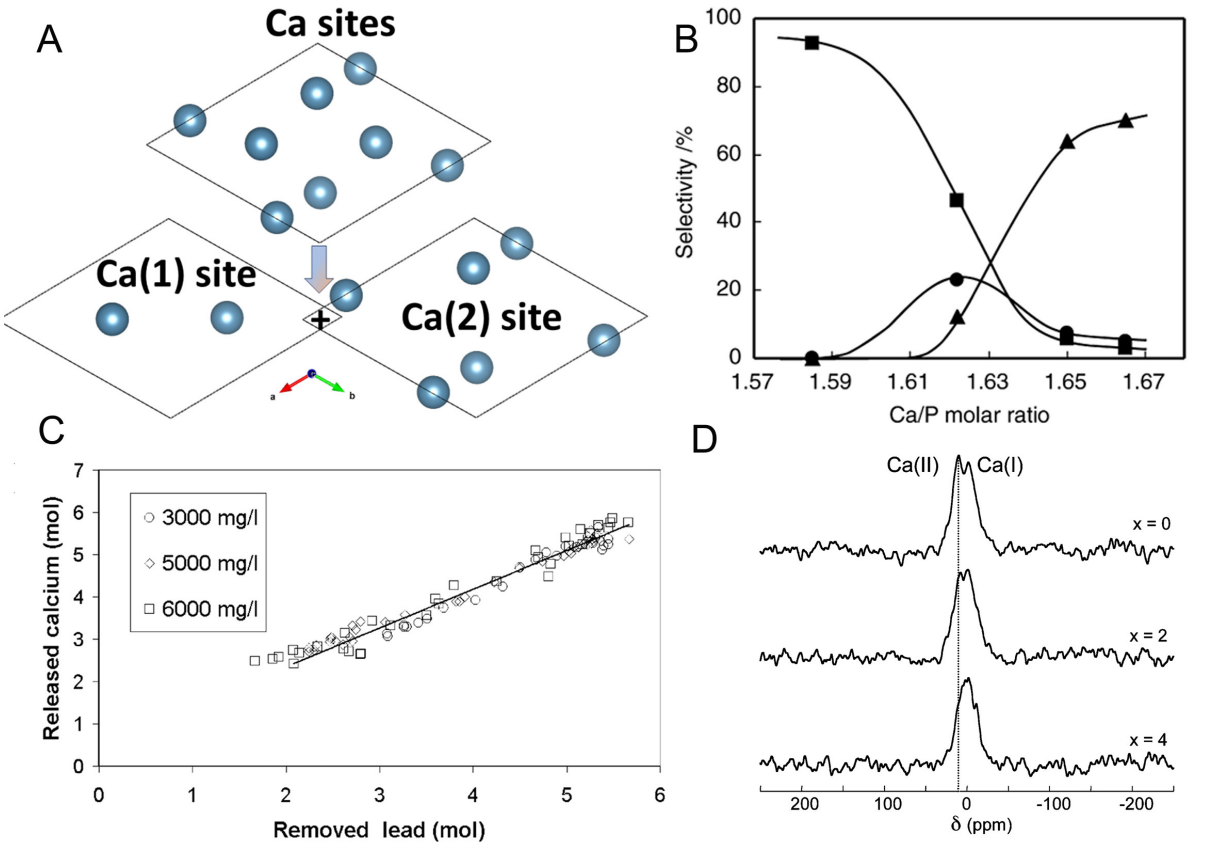

Figure 2. (A) HAP hexagonal crystal structure unit cell with two Ca sites, $Ca_{(I)}$ and $Ca_{(II)}$ sites. Reproduced from Ref.[18] under CC BY 4.0 license. (B) Product selectivity at 50% ethanol conversion: (▲) total Guerbet alcohols, (●) 1,3-butadiene (■), ethylene. Reproduced from Ref.[19] with permission from Elsevier. (C) Moles of Ca^{2+} released to the solution as a function of moles of Pb^{2+}. Reproduced from Ref.[20] with permission from Elsevier. (D) ^{43}Ca MAS spectra of $Pb_xCa_{10-x}(VO_4)(PO_4)_5(OH)_2$ (x = 0, 2, 4). Reproduced from Ref.[21] with permission from American Chemical Society.

column structure that defines two types of discrete channels. The first channel has a diameter of 2.5 Å with adjacent Ca^{2+} ions. The adjacent Ca^{2+} ions are in the $Ca_{(II)}$ location and these Ca^{2+} play a significant role in modulating the acid-base and electrical properties of HAP material. HAP allows large variations in composition and can be a highly non-stoichiometric solid. Stoichiometric HAP has the chemical formula of $Ca_{10}(PO_4)_6(OH)_2$ where the ratio Ca/P is 1.67. Non-stoichiometric HAP has Ca/P < 1.67 with chemical formula of $Ca_{10-x}(HPO_4)_x(PO_4)_{6-x}(OH)_{2-x}$ where $0 < x < 1$. The OH^- groups are arranged along the c-axis in the HAP unit cell to balance the positive charge of the matrix. The substitution of cations or anions within the lattice can lead to vacancy defects at calcium or OH^- sites. Alternatively, such substitutions may induce structural disorder, resulting in the formation of an amorphous phase.

The stoichiometric HAP crystals can exist in two forms: hexagonal (lattice parameters a = b = 9.432 Å, c = 6.881 Å, and γ = 120°) and monoclinic (lattice parameters a = 9.421 Å, b = 18.840 Å, c = 6.881 Å, and γ = 120°)[22-24]. To maintain charge balance in the lattice and surface, the two polymorphs exhibit different surface OH orientations. In the monoclinic form, all the OH groups face in the same direction. As for the hexagonal HAP, the adjacent OH points in opposing directions[24]. The transformation from the monoclinic phase to the hexagonal phase can occur due to synthesis methods, temperature change, and cation exchange[22-24]. The transition from a hexagonal structure to a monoclinic structure is found to be reversible so long the annealing temperature does not go beyond 200 °C[25]. The poly-morphology of metal oxide catalysts can influence catalytic activity and product selectivity as reported by several authors[26,27]. For example, when Ru is deposited onto different phases of TiO_2 - rutile, anatase, or a mix of both, the crystal facets of the TiO_2 support can affect the extent of metal-support interaction and modify the nature and activity of Ru species for CO_2 methanation[28]. In a similar analogy for the HAP catalyst support, different crystal structures exhibited by the HAP catalyst support can influence catalytic activity and product selectivity - we elaborate on this in later sections. Hence, this unique property of the HAP structure can be used to engineer the HAP surface for enhanced catalytic activity and product selectivity.

Importance of the Ca/P ratio

As the apatite material consists of calcium cation and phosphate anion in the unit cell, the surface properties of the apatite material are intimately connected to the apatite surface composition. When the Ca/P is at a stoichiometric ratio of 1.67, there are more basic sites than acidic sites, which results in HAP displaying basic catalyst behavior. HAP surface displays acidic behavior when the Ca/P = 1.50, which constitutes a non-stoichiometric HAP. The mix of basic and acid sites imbues the catalyst surface with amphoteric properties if the Ca/P is between 1.5-1.67. However, it is also important to note that the bulk Ca/P ratio is observed to be greater than the surface Ca/P ratio[19]. Thus, the HAP surface can be non-stoichiometric in nature. HAP crystal tends to grow along the c-axis (i.e., rod-like HAP) and expose more of the a-faces, which are rich in Bronsted acid phosphate groups[19].

The implications of the Ca/P ratio on the surface properties of the HAP support material can be observed from the differences in catalytic activity and product selectivity as noted by several authors[19,29,30]. HAP had been used as a catalyst for Guerbet alcohol synthesis, wherein the presence of more acidic sites in HAP catalyst at varying Ca/P has shown a clear influence in favoring ethylene selectivity while more basic sites favor 1-butanol selectivity as shown in Figure 2B[19]. If an active transition metal such as nickel is incorporated into the HAP support, the Ca/P can also be varied to induce CaO to exsolve from the HAP surface which can help to tune metal-support interaction effects[31,32]. Furthermore, the decrease of Ca/P can induce the presence of more acidic sites which can help to anchor the nickel nanoparticles onto the HAP support, thus improving catalyst stability.

Cationic substitutability

The calcium cation site in the apatite unit cell is flexible enough to accommodate transition metal cations that are similar to its ionic radii. The calcium cations in $Ca_{(I)}Ca_{(II)6}(PO_4)_6(OH)_2$ HAP are situated in two different places in the framework, $Ca_{(I)}$ and $Ca_{(II)}$. The coordinating number of the $Ca_{(I)}$ is 9, while the one for $Ca_{(II)}$ is 7. Such a difference suggests that $Ca_{(I)}$ would be preferentially occupied by other cations larger than Ca^{2+}[33]. Transition metal cations can be incorporated into the HAP framework using coprecipitation or ion-exchange methods. In coprecipitation, two aqueous solutions are typically prepared, one with Ca^{2+} and cation, and another with the phosphate precursor. The pH of both solutions should be similar for concurrent precipitation of Ca^{2+} and P.

The calcium sites in the HAP lattice are also amenable to substitution by another cation from transition metal elements or lanthanide elements[34]. The calcium sites can be substituted by monovalent (e.g., Na^+, K^+, Ag^+, *etc.*), divalent (e.g., Cu^{2+}, Ni^{2+}, Zn^{2+}, *etc.*), and trivalent (e.g., Ce^{3+}, Co^{3+}, *etc.*) metals. However, the extent of difficulty in substituting the Ca sites could be dependent on the electronegativity of the element, assuming the same ionic radius[35]. For monovalent cations such as Na^+, K^+, and Li^+, Na^+ has a better affinity for cation substitution into the HAP lattice due to similar ionic radii as Ca^{2+} (0.9 Å). Thus, the order of affinity decreases in the following manner: Na^+ (1.0 Å) > K^+ (1.4 Å)> Li^+ (0.7 Å)[36]. The preference for cation exchanges due to differences in ionic radii relative to the Ca^{2+} ionic radii is similar for divalent components. Takeuchi *et al.* observed that Pb^{2+} was exchanged faster than Cu^{2+} and Cd^{2+} due to the same ionic radii as Ca^{2+} in the single-component adsorption study[37]. In a dual-component adsorption study, the Cu^{2+} was more difficult to exchange with Ca^{2+} and was attributed to the bigger ionic radii of Cu^{2+} (1.3 Å) as compared to Ca^{2+} (1.1 Å). However, Cd^{2+} (1.1 Å), being of the same ionic radii as Ca^{2+}, was also more difficult to exchange because of lower electronegativity than Pb^{2+}. Furthermore, the hydrated Cu^{2+} and Cd^{2+} ions need to be dissociated before exchanging with Ca^{2+}. Thus, there is a possible additional rate-determining step that slows the rate of ion exchange. Further observation by Bailliez *et al.* noted that the Pb^{2+} cations have largely occupied the $Ca_{(II)}$ position to form $Pb_{10-x}Ca_x(PO_4)_6(OH)_2$ solid solution[20]. In Figure 2C, the gradient of the slope is close to unity, which indicates an equimolar exchange of Pb^{2+} and Ca^{2+} cations. The Pb^{2+} cations are first adsorbed onto the HAP surface, especially the POH group, via surface complexation, which occurs very quickly. After complexation, Pb concentration saturates and slows down. Adsorption continues due to the high surface area of HAP powder but at a slower rate as the surface adsorption approaches equilibrium. The HAP surface may be heterogeneous, meaning some areas have lower affinities for Pb^{2+} cations[20]. The Langmuir-Freundlich model fits better than the Langmuir or Freundlich models, suggesting a heterogeneous HAP surface with varying affinities for cationic adsorption. This indicates two things: first, cations adsorb onto the HAP surface as a monolayer through an ion-exchange mechanism. Second, multiple active sites participate in cation adsorption and integration into the HAP lattice via cation substitution, explaining the Langmuir-Freundlich fitting results[38].

Various cations with differing ionic radii can alter unit cell dimensions when replacing calcium. For example, substituting Ca^{2+} with Mg^{2+} decreases the lattice constant c by 0.33% and increases constant a by 0.1%, leading to significant lattice disturbances and possibly more defects in HAP surfaces[39]. Introducing metal cations smaller than Ca shrinks the lattice unit cell and increases the X-ray diffraction (XRD) Bragg angle, resulting in smaller HAP size and greater irregularity shape. Cu^{2+} and Zn^{2+} preferentially substitute at the $Ca_{(II)}$ to form a 4 to 5-fold coordination with the HAP support[40]. Solid-state nuclear magnetic resonance (NMR) can be used to determine whether the cation substitutes at the $Ca_{(I),}$ or $Ca_{(II)}$ site. Pizzala *et al.* used solid-state NMR and observed chemical shift in ^{43}Ca NMR, as compared to pure HAP phase, for different concentrations of substituting cations of Pb and V, as shown in Figure 2D[21]. Another technique to confirm cationic substitution is Raman spectroscopy. The characteristic peak belonging to PO_4^{2-} can be shifted to a lower Raman shift if the Ca cation is substituted with another metal cation. For divalent cations with larger

ionic radii, such as Pb^{2+}, the substitution increases both lattice constant a and c by around 0.05% and 0.04%, respectively[35]. These changes in the crystal lattice parameters often cause changes in crystallinity, thermal stability, and morphology and may influence product selectivity in DRM and thermal catalytic CO_2 hydrogenation reactions[41].

Ionic radii depend on valence electron density and the effective nuclear charge of cations. For the same nuclear charge, higher valence charge leads to smaller ionic radii due to stronger electrostatic attraction. Conversely, decreased valence charge results in larger ionic radii. Structural defects may form to accommodate other metal ions and maintain charge neutrality. HAP uniquely preserves the crystallographic symmetry of P63/m even when Ca/P drops below 1.67. Density functional theory (DFT) computational studies provide insights into HAP structure, indicating how different cations substitute in $Ca_{(I)}$ or $Ca_{(II)}$ sites[42]. Ellis *et al.* combined DFT with experimental methods such as X-ray absorption near edge structure (XANES) and extended X-ray absorption fine structure (EXAFS) to identify the preferred Ca site for Pb substitution, demonstrating that Pb^{2+} favors the $Ca_{(II)}$ sites[43].

For trivalent cations such as Ce^{3+}, Fe^{3+}, and Al^{3+}, which have ionic radii slightly larger than Ca^{2+}, the extent of cation substitution into the HAP lattice is again dependent on the electronegativity of the cations. The coprecipitation method was utilized to synthesize the cation-substituted materials. The authors observed morphological changes by adding different trivalent components[44]. The ones added with Fe^{3+} had a longer nanorod morphology than those of Al^{3+} and La^{3+}. Furthermore, the addition of such trivalent elements into the HAP lattice brought about reduced crystallinity, as observed from the XRD data. This indicates that ion-exchanged HAP, be it through coprecipitation or immersion, becomes either more amorphous or has reduced particle size. Although La^{3+} has similar ionic radii to Ca^{2+}, the order of ionic substitution goes in the following order: $Al^{3+} = Fe^{3+} > La^{3+}$. The charge density goes in the following order: $Al^{3+} > Fe^{3+} > La^{3+}$. Hence, the extent of ion exchange with such trivalent cations appears to be dependent on the component charge density. Cerium can also be substituted into the HAP lattice to create highly amorphous HAP phases[45]. Furthermore, as the ionic radius of Ce is larger than Ca^{2+}, the lattice constants a and c are observed to increase with a corresponding increase in Ce concentration[46]. A possible reason behind the amorphousness of the Ce-HAP could be the presence of mixed Ce^{3+} and Ce^{4+} cations in the HAP lattice, which creates a higher concentration of oxygen vacancies on the HAP surface. The presence of oxygen vacancies that would be beneficial in several catalytic reactions will be discussed in later sections.

Anionic substitutability

The HAP structure contains two anionic sites located at the OH^- group and the PO_4^{2-} group. The most common anionic substitution is the carbonate anionic substitution. In such anionic substitution, the surface hydroxyl (OH^-) is substituted with the carbonate group (CO_3^{2-}), also known as A-site substitution. The A-site substitution results in the HAP chemical formula in the following manner: $Ca_{10}(PO_4)_6(OH)_{2-2k}(CO_3)_k$. Another form of anionic substitution is the substitution of the phosphate group. The phosphate group (PO_4^{2-}) in the HAP structure can also be substituted by other anions such as F^-, Cl^-, SiO_4^{4-}, and CO_3^{2-}. This is known as B-site substitution. This results in the HAP chemical formula being written in the following order: $Ca_{10-v}(PO_4)_{6-v}(CO_3)_v(OH)_{2-v}$, where $0 < v < 2$. The CO_3^{2-} substitution in the B-site can cause an expansion of the c-axis and contraction of the a-axis as the ionic radius of the CO_3^{2-} group is larger than the phosphate group[47]. The location of CO_3^{2-} substitution can be observed from Fourier Transform Infrared Spectroscopy (FTIR) spectra as the peak assigned to OH^- will be diminished if the CO_3^{2-} group substitutes the surface OH^-[48]. Furthermore, CO_3^{2-} substitution has been observed to cause a reduction in crystallinity and resultant smaller particle size. In addition, the partial substitution of the phosphate group with the carbonate group enables more facile cationic substitution due to more electrons withdrawn from the Ca cations[40].

Anionic substitution at either of these two sites can tune surface acidity. CO_3^{2-} substitution at the A site can create two types of acid sites: strong acid sites from the ring of Ca^{2+} cations and very strong acid sites ascribed to proton contribution from the HPO_4^{2-} group[48]. CO_3^{2-} substitution can create lattice mismatch as CO_3^{2-} is larger than OH^- but smaller than PO_4^{2-}[49]. As the surface acidity is altered by the presence of anionic substitution of the apatite cell structure, the catalytic activity and product selectivity can be altered. If F^- is substituted into Pb-HAP, the catalytic activity for oxidative coupling of methane can be favored towards ethylene as more electrons are donated to stabilize methyl intermediate[41]. Further discussion on the effect of anionic substitution on catalytic activity will be provided in the later sections.

SUSTAINABLE CHEMICAL AND ENERGY PRODUCTION

Sustainable chemical production

Oxidative CH_4 coupling to higher order hydrocarbon

Higher order hydrocarbon (OCM) has been a "holy grail" for economically viable methane conversion into ethylene and ethane for decades since Lunsford's seminal paper[50]. Traditional OCM catalyst includes promoted silica-based systems and rare-earth oxides to give ca. 20%-30% C_2 yield and around ~80 C_2 selectivity[51,52]. Importantly, basicity is one key strategy to stabilize methoxy radicals with optimal binding strength for C_{2+} hydrocarbon formation[52,53]. In recent years, HAP-based catalysts, especially Pb-substituted HAP, with appropriate synthesis procedures and treatment, have been demonstrated to be active for OCM to produce ethane and ethylene [Table 1], to achieve around 22% C_2 yield (35% CH_4 conversion and 62% C_2 selectivity) at 775 °C[54]. This performance is about five-fold higher selectivity than the undoped HAP, highlighting the promotional effect of Pb. Pb^{2+} sites doped in HAP were found to moderate active oxygen species [i.e., higher surface basicity confirmed by CO_2-temperature-programmed desorption (TPD) study] and aid in stabilizing key intermediate methoxy radicals, preventing their premature oxidation to CO_x. In addition, Pb improves structural stability; for example, in Ca-Pb HAP, the intact apatite structure is preserved during reaction, preventing deactivation and maintaining active O- sites[55]. Other dopants have also been considered, including Sr, Ba, and Ca, but studies revealed that mono-dopants yield poor OCM activity, with the exception of Pb-substituted HAP[56,57]. The strategy is therefore shifting toward co-doping, where a secondary dopant (e.g., Pb, Cl^-, or Zr) is introduced to balance surface basicity, enhance methyl radical coupling, and stabilize the apatite framework under high-temperature oxidative conditions.

Oxidative propane dehydrogenation

Commercial propane dehydrogenation is an endothermic catalytic reaction that produces propylene as a valuable chemical intermediate. Thermal energy input is required to drive the catalytic reaction, incurring CO_2 emissions[61]. Although the CO_2 emission for commercial propane dehydrogenation is lower than steam cracking of naphtha, there is still a need to lower the CO_2 emission by making the process more exothermic using oxidants such as O_2 and CO_2[62,63]. This makes the process more sustainable and commercially viable. However, when oxidants such as O_2 are used, the propylene selectivity becomes greatly reduced and the catalyst becomes easily oxidized and sintered; thereby, deactivating the catalyst over time[64]. Hence, it is crucial to explore alternative materials for catalyst development for this catalytic reaction.

For oxidative propane dehydrogenation catalyst, V/SiO_2 exhibited a reasonably good performance of 5% propane conversion and 66% propylene selectivity[65]. HAP-based catalysts displayed around 5% propane conversion and 26.4% propylene selectivity as seen in Table 2. HAP facilitates C-H bond activation through its inherent basic sites, particularly surface OH^- groups and phosphate units, which promote the initial hydrogen abstraction from propane. Additionally, the incorporation of metal ions (e.g., Co^{2+} and Cr^{3+}) into the HAP lattice modifies its redox and acid-base properties. For example, Co-doped HAP facilitates hydrogen abstraction via surface OH^- group[66], whereas Cr-substituted HAP enhances release of lattice

Table 1. Catalytic performance of HAP-based catalysts for oxidative coupling of methane (OCM)

Catalyst	WHSV (mL/gcat.h)	T (°C)	Pressure (bar)	Feed composition	CH_4 conversion (%)	C_2 and (CO_2) selectivity (%)	Stability (mins)	Reference
$Pb_2Ca_8(PO_4)_6(OH)_{0.5}Cl_{1.5}$	6,000	740	1	$P(CH_4)$ = 21.6 kPa $P(O_2)$ = 10.8 kPa	35	62(n.r.)	3,600	[54]
	Remarks: Chloro-HAPs were prepared with Pb substituted in HAP framework to optimize basicity, a key characteristic feature for determining OCM activity							
Ca9.5Pb0.5	6,186	800	1	$P(CH_4)$ = 21.8 kPa $P(O_2)$ = 10.9 kPa	40	55(n.r.)	2,400	[55]
	Remarks: Hydroxyapatites with optimal Pb substitution (i.e., Ca9.5Pb0.5; $Ca_{(10-x)}Pb_x(PO_4)_6(OH)_2$, x = 0.5) exhibited the best performance due to improved thermal structural integrity							
SrC1ZrP(13/4)	6,000	750	1	$P(CH_4)$ = 16.5 kPa $P(O_2)$ = 8.3 kPa	25	52(n.r.)	3,000	[56]
	Remarks: Promoted strontium chlorapatite [$Sr_{10}C_{12}(PO_4)_6$] has relatively thermally stable SrCl to increase the concentration of alkali beneficial for OCM							
CaHAP-PbHAP	3,600	700	1	$P(CH_4)$ = 28.7 kPa $P(O_2)$ = 4.1 kPa	18	80(n.r.)	1,440	[57]
	Remarks: CaHAP-PbHAP containing 30 wt.% PbHAP exhibited the best performance, attributed to the synergistic interaction between CaHAP and PbHAP, where CaHAP actively facilitates hydrogen abstraction from methane, while PbHAP stabilizes the resulting methyl radicals							
Pb-HAP-CO_3	9,200	700	1	$P(CH_4)$ = 27.1 kPa $P(O_2)$ = 11.0 kPa	~25	35(65)	600	[58]
	Remarks: The substitution of Pb into the HAP crystal structure stabilizes methyl radicals for C_2 product formation, while the CO_3 group improves the catalytic stability of the catalyst							
Pb-HAP (0.1)	3,000	700	1	$P(CH_4)$ = 29.0 kPa $P(O_2)$ = 4.0 kPa	~14.5	~20(20)	180	[59]
	Remarks: The addition of Pb was observed to improve C_2 selectivity due to the stabilization of methyl radicals to form C_2 products							
Pb-HAP (c-surface)	34,300	700	1	$P(CH_4)$:$P(O_2)$ = 4:1, unspecified N_2 dilution	~5.0	~35(35)	600	[60]
	Remarks: The c-surface on Pb-HAP enables the more facile formation of hydroxyl vacancies which can absorb molecular O_2 and make the stabilization of methyl radicals more energetically favorable. This results in higher C_2 selectivity in OCM							

WHSV: Weight hourly space velocity; n.r.: not reported.

oxygen for hydrogen abstraction[67]. The propylene selectivity is still lower than the V/SiO_2 benchmark catalyst. Hence, more research effort is required to enhance propylene selectivity through a more rational understanding of the catalyst surface.

Biodiesel production

Diesel is derived from petroleum distillation and is widely used in vehicle transportation. Biodiesel production from renewable sources is strongly considered a more sustainable pathway than oil-derived diesel. Biodiesel comprises fatty acid alkyl esters (FAME) which can be synthesized from vegetable oil or animal fats

Table 2. Catalytic performance of HAP-based catalysts for oxidative propane dehydrogenation

Catalyst	WHSV (mL/gcat.h)	T (°C)	Pressure (bar)	Feed composition	C_3H_8 conversion (%)	C_3H_6 selectivity (%)	Stability (mins)	Reference
Co55SrHAP	3,600	450	1	$P(C_3H_8)$ = 14.5 kPa $P(O_2)$ = 4.1 kPa	22.1	48.6	360	[66]
	Remarks: The integration of Co^{2+} into the Sr-HAP lattice encourages hydrogen abstraction due to easier removal of H from the surface OH^- group							
Cr(3.7)/CaHAP	90,000	550	1	$P(C_3H_8)$ = 6.08 kPa $P(O_2)$ = 3.04 kPa	~20.0	~34.0	300	[67]
	Remarks: The Cr species on the HAP surface become more oxidized after calcination in the presence of air into Cr^{6+}. Cr^{6+} was eventually reduced to Cr^{3+} during the reaction. The presence of Cr^{3+} favors the release of lattice oxygen which is important for hydrogen abstraction for propylene formation							
V-CaHAP (V/P = 15) re-oxidized	3,600	450	1	$P(C_3H_8)$ = 14.5kPa $P(O_2)$ = 4.1 kPa	15.2	55.2	360	[68]
	Remarks: The redox cycling between V^{4+} and V^{5+} and lattice oxygen (abstraction and incorporation) are important in propane conversion and propylene formation							
$Ca_{10}(PO_4)_{0.78}(VO_4)_{5.22}(OH)_{1.32}O_{0.34}$	7,500	450	1	$P(C_3H_8)$ = 7.5 kPa $P(O_2)$ = 2.13 kPa	~5.0	~27.0	90	[69]
	Remarks: The formation of vanadium oxy-HAP created basic sites that are essential for activating the C-H bonds in propane molecules							

WHSV: Weight hourly space velocity.

via a transesterification reaction with methanol as the reactant[70]. Waste cooking oil can be used as an alternative feedstock which lowers biodiesel production costs[71]. Basic homogeneous catalysts such as NaOH and KOH are effective for biodiesel production but pose challenges such as corrosiveness, difficult separation, and wastewater generation[72], while solid CaO offers recyclability and high yields, but suffers from deactivation by CO_2/H_2O and leaching due to reaction with glycerol[73,74]. HAP-based catalysts demonstrate several innovations that address the key limitations of conventional CaO-based systems in biodiesel production. Notably, HAP provides excellent surface basicity and structural stability, enabling a high biodiesel yield of 95% for eight cycles with negligible leaching as seen in Table 3; hence, HAP-based catalysts deserve closer research attention[75].

Hydrogen production

Dry reforming of methane (DRM)

Catalytic transformation of greenhouse gases such as CO_2 and CH_4 to produce syngas is highly desirable as syngas can be used as feedstock for the Fischer-Tropsch process, methanol synthesis, and one-step dimethyl ether (DME) synthesis process[83]. Thus, it can be considered a sustainable path for syngas production. Syngas can also be used as a source of hydrogen or directly to produce electricity[84,85]. DRM, which uses CO_2 as a feedstock, is a desirable alternative to current syngas generation processes from an environmental and sustainability perspective[86]. A major technical challenge in DRM is rapid catalyst deactivation induced by severe coke formation during the reaction, which hinders the commercial development of the DRM process[87]. The last decade has thus seen vigorous research in catalyst development for this process to increase activity, stability, and resistance to coking[88].

Table 3. Catalytic performance of HAP-based catalysts for biodiesel production

Catalyst	T (°C)	Feed condition	Conversion (%)	No of cycles	Reference
30K/HAP-600	65	30 g of palm oil and an appropriate amount of methanol	96.4	8	[75]
	Remarks: The synergistic effect of K_2CO_3 addition and calcination at 600 °C maximized surface basicity; thus, maximized FAME yield for 8 reaction cycles at ca. 90%. Slight deactivation occurred due to K^+ leaching				
Ni-Ca-HAP	70	The waste fish scale has a high acid value	59.9	2	[76]
	Remarks: The Ni-Ca-HAP solid acid catalyst can be applied to convert high acid value feedstock into biodiesel (FAME) compared with the calcined waste fish scale (WFS) "base catalyst". The Design of Experiment methodology was applied and revealed that methanol flowrate and nickel nitrate loading are the most important parameters in maximizing FAME yield				
11 wt.% dosage of 30%CaO-CeO_2/HAP-650	65	30 g of palm oil with a 9:1 methanol to palm oil molar ratio	91.84	8	[77]
	Remarks: The synergistic addition of CaO-CeO_2 onto bone-derived HAP enhanced FAME yield in 8 reaction cycles due to higher basicity. The leaching concentration dropped over more cycles due to lattice distortion by Ca^{2+} and Ce^{4+} substitution. The specification of the produced biodiesel is within the ASTM standard for biodiesel				
5%CaO-HAP	60	100 g of vegetable oil	95.18	4	[78]
	Remarks: The bone-derived HAP support possessed a higher BET area than pure CaO, even though CaO is postulated as the active site. The extent of CaO penetration into the HAP pores or CaO dispersion on the HAP surface may be evaluated using visual characterization techniques such as TEM				
50-NaHAP-800	100	Methanol to oil molar ratio of 6:1	99	5	[79]
	Remarks: Sodium nitrate loading and calcination temperature were found to be important in maximizing FAME yield by enhancing surface basicity. The produced biodiesel meets EN14214 standards				
HAP-γ-Fe_2O_3	65 (methanol reflux temperature)	Methanol/soybean oil molar ratio of 25:1	94	5	[80]
	Remarks: HAP was encapsulated around γ-Fe_2O_3 via the coprecipitation method to form a core-shell nanoarchitecture before immobilizing with biguanide molecules. The soybean conversion to methyl ester is close to 100% for 5 cycles with little deactivation. The catalyst can be recycled due to the strong magnetic properties of the γ-Fe_2O_3 core				
Marble slurry-based HAP	65	Methanol/soybean oil molar ratio 9:1	94	5	[81]
	Remarks: HAP is found to be a better catalyst than calcined marble slurry (CMS) for biodiesel production in terms of biodiesel yield and fuel properties because of higher basicity (13.30 mmol/g for HAP and 9.23 mmol/g for CMS). The produced biodiesel meets the ASTM D6751 standards				
HAP	65	The canola oil, rapeseed oil, and waste cooking oil to methanol molar ratio was taken as 1:12	89.4%, 96.7% and 91.7% were achieved for canola oil, rapeseed oil, and waste cooking oil, respectively	-	[82]
	Remarks: The synthesized catalyst showed high total basicity after calcination				

WHSV: Weight hourly space velocity.

Conventionally, Ni/$MgAl_2O_3$ catalysts were commonly used as a benchmark, which exhibited 90% CH_4 conversion and approx. 92% CO_2 conversion at 750 °C[99]. HAP-based catalysts have been shown to outperform the benchmark catalyst with 90% CH_4 conversion and approx. 95% CO_2 conversion for 24 h at 750 °C[89]. One Ni-HAP catalyst prepared using the one-pot synthesis method can produce a stable catalytic performance of 200 h[90]. HAP-based catalysts for

DRM reaction present opportunities to enhance catalytic performance and stability by adjusting surface basicity, porosity, and metal-support interaction. Strategies such as coprecipitation, incorporation of secondary metals (e.g., Co, Ce), or use of structure-directing agents have been shown to enhance Ni dispersion, prevent sintering, and promote single-atom configurations, leading to improved resistance against coking [Table 4]. Moreover, non-stoichiometric HAP and doped HAP variants allow for oxygen vacancy formation and lattice substitution, which are crucial for redox-driven activation of CO_2 and stabilization of reactive intermediates.

Partial oxidation of CH_4 (POM)

The current technology for syngas production, methane steam reforming ($\Delta H°_{298}$ = 206.0 kJ/mol), requires a tremendous amount of energy to break the C-H bond in methane and the O-H bond in steam. As a result, the CO_2 emission per hydrogen produced (i.e., 11.5 tons CO_2 emitted per ton H_2) is the highest among the available technologies, such as natural gas-fired methane pyrolysis and electric-arc furnace methane pyrolysis for hydrogen production and creates a strong motivation to move towards a more sustainable hydrogen production[100].

POM is an attractive alternative to the commercial steam reforming of methane reaction as it is an exothermic reaction, and a high H_2/CO ratio (~2) can be attained. Higher H_2/CO is advantageous for Fischer-Tropsch, solid oxide fuel cells, and methanol synthesis from CO hydrogenation[101]. The technical issues with POM are that full methane combustion can occur as a side reaction, which can reduce the H_2/CO ratio and metal sintering due to exothermic heat from the reaction. HAP had been used as a catalyst support for POM and exhibited reasonable catalytic performance. The benchmark catalyst for POM, Ni-Mg-Al hydrotalcite, showed 88.4% CH_4 conversion and 86.2% H_2 yield at 750 °C. The HAP-based catalyst (as seen in Table 5) can attain up to around 90% CH_4 conversion and 90% H_2 yield at 750 °C, which is very similar to the hydrotalcite catalyst[102]. The similarity in catalytic performance justifies the effort in further exploration of HAP-based catalysts for POM.

CO oxidation

CO oxidation is an integral reaction to eliminate CO in hydrogen fuel applications and emission control in automobile applications to meet government emission standards[113]. Hence, it is an important reaction that can speed up the use of hydrogen fuel cells and make transportation more sustainable. Typically, noble metals such as Au have shown to be effective in creating highly active sites for CO oxidation due to the formation of cationic Au and metallic Au, and this may enhance O_2 dissociation at the metal-support interface[114-116]. The HAP-based catalyst is seven times more active than the benchmark catalyst (Au/Fe_2O_3) (i.e., 0.071 mol_{CO}/g_{Au}·h *vs.* 0.011 mol_{CO}/g_{Au}·h) [Table 6][117]. The excellent catalytic performance indicates that HAP-based catalysts deserve more careful investigation to develop an active and stable catalyst for this reaction

Water gas shift reaction

Currently, the WGS reaction is employed to increase the H_2/CO ratio of syngas produced from the steam methane reforming (SMR) process. Thereby enhancing the sustainability of the SMR process. The commercial WGS catalysts used are the Fe-Cr mixed oxide catalyst and the Cu-Zn mixed catalyst used at a high-temperature range (350-450 °C) and a lower temperature range (190-250 °C), respectively[124]. As the WGS reaction is restricted by thermodynamic equilibrium, the commercial catalytic process typically performs the reaction at high temperatures, followed by a lower temperature range to increase CO conversion and H_2 yield, thus approaching thermodynamic limits. Although the Fe-Cr mixed oxide catalyst displayed moderate catalytic performance suitable for industrial purposes, it is important to note that there

Table 4. Catalytic performance of HAP-based catalysts for dry reforming of methane

Catalyst	WHSV (mL/gcat.h)	T (°C)	Pressure (bar)	Feed composition	CH_4 conversion/CO_2 conversion (%)	H_2/CO ratio	Stability (h)	Carbon formation (%wt.)	Reference
$2Ni_1$/HAP-Ce	60,000	750	1	20 mol%CH_4 20 mol%CO_2 60 mol%He	~95/80	~0.8	100	~0	[89]
	Remarks: Ce-doping induces strong metal-support interaction which anchors the Ni cluster and single atoms and activates the C-H bond in methane. This results in high activity and stability for 100 h with near negligible carbon formation								
$Ni_{0.5}$/HAP-OP	30,000	800	1	10 mol%CH_4 10 mol%CO_2 80 mol%N_2	93.3/98.8	1.0	200	~0	[90]
	Remarks: The coprecipitated Ni/HAP catalyst displayed very high reactant (CO_2 and CH_4) conversion due to the quick conversion of CH_4 into carbon and H_2. The carbon gasification into CO is equally quick, resulting in negligible carbon accumulation on the catalyst surface. The surface basicity of the catalyst requires more careful investigation								
Ca-HAP2	15,900	700	1.6	20 mol%CH_4 20 mol%CO_2 60 mol%N_2	78/84	n.r.	90	n.r.	[91]
	Remarks: The Ni-HAP catalysts with different surface areas displayed comparable catalytic activity and stability with existing literature of that time due to small Ni nanoparticle size, surface basicity, and large surface area (66 m^2/g_{cat}). But no results on carbon formation and H_2/CO ratio for the two catalysts were shown								
Co-HAP-N	31,764	700	1.6	20 mol%CH_4 20 mol%CO_2 60 mol%IN_2	75/55	~0.75	50	~10	[92]
	Remarks: The non-stoichiometric Co-HAP catalyst performed better than the stoichiometric Co-HAP. The carbon formation for the NiCo-HAP catalyst was lower than the Co-HAP or Ni-HAP catalyst								
Ni(4)/CaHAP	38,400	600	1	3 mol%CH_4 3 mol%CO_2 94 mol%IN_2	78/78	~0.70	4	~50	[93]
	Remarks: Three types of Ni species were observed on the surface using H_2-Temperature Programmed Reduction (TPR). A Higher amount of Ni^{2+} was substituted into the HAP lattice at lower Ni loading. With the increasing amount of Ni loading, more NiO is formed and therefore less Ni^{2+} is available for cation substitution into the HAP lattice. Carbon formation correspondingly increases with Ni loading								
Ni-Co/HAPSIWI	8,823	750	1.6	20 mol%CH_4 20 mol%CO2 60 mol%N_2	73/79	~0.90	160	< 13	[94]
	Remarks: Bimetallic Ni-Co species were present and cation-exchanged onto the HAP support for good and stable catalytic performance. A limited amount of carbon was observed on the catalyst surface using TEM characterization but was not quantified using the TGA technique								
Pt-HAP	8,400	700	1	20 mol%CH_4 20 mol%CO_2 60 mol%N_2	40/30	~0.81	50	n.r.	[95]
	Remarks: Ru and Pt-based HAP catalysts were prepared using different deposition methods such as incipient wetness impregnation method, cation exchange, and excess liquid impregnation. The one prepared by incipient wetness impregnation displayed reasonable catalytic performance over time than other methods. A water trap was used to quantify water formation over time								
$0.5Ni_1$/HAP-	60,000	750	1	20 mol%CH_4	~75/85	~0.9	16	~0	[96]

SAC-PVP				20 mol%CO_2 60 mol%He					
	Remarks: The Ni-HAP assisted by PVP addition exhibited good catalytic performance over time due to the greater prevalence of Ni single atoms. The authors did not further expound on the role of PVP in enhancing the catalytic performance and stability of the Ni single atom on the HAP catalyst surface								
Ni/HAP-80	24,000	750	1	50 mol%CH_4 50 mol%CO_2	44/55	~0.77	~12	0.99	[97]
	Remarks: The ratio of mesopores and macropores of HAP can be controlled when the heating temperature varies in the presence of cetyltrimethylammonium bromide (CTAB). This ratio can influence the Ni particle size which can affect catalytic performance and stability								
Ni/Ca-HA1_S	15,882	700	1	50 mol%CH_4 50 mol%CO_2	50/60	0.8-0.9	30	< 10	[98]
	Remarks: The regeneration property of the Ni-HAP catalysts in different oxidizing atmospheres (O_2 and CO_2) was investigated. There is a very small decrease in the CH_4 conversion of the Ni-HAP catalyst over three cycles. The reason for the decrease in catalytic activity could be Ni nanoparticle sintering during the reaction								

WHSV: Weight hourly space velocity; n.r.: not reported.

is strong regulatory pressure to replace the Fe-Cr mixed oxide catalyst as Cr^{6+} is highly carcinogenic and can cause immense harm to human life and the natural environment[125]. These concerns have motivated intense research to explore alternative materials that exhibit high catalytic performance and yet are less harmful to human life and the natural environment. A work by Miao *et al.* demonstrated that HAP-based catalysts can display better catalytic performance than CeO_2-based catalysts in WGS, as a consequence of the unique HAP structure where H_2O could be polarized by Lewis acidic Ca^{2+} ions and H bonding to basic O atoms of PO_4^{3-} units[126]. Thus, the HAP-based catalyst deserves detailed investigation to improve WGS catalytic performance.

CO_2 utilization

CO_2 hydrogenation to CH_4

As the mitigation of CO_2 emissions becomes a pressing issue globally, CO_2 utilization technologies via thermal and photothermal means have gathered momentum in recent years[127]. CO_2 hydrogenation to methane (i.e., CO_2 methanation) has gained increasing attention as an alternative method to produce sustainable methane while reducing CO_2 emissions at the same time[128-130]. HAP has gained traction as an alternative support in CO_2 methanation[131]. As photothermal CO_2 reduction is still in a nascent stage of development, significant effort is required to develop an active, stable, and selective catalyst before scaling-up efforts can be undertaken[132]. The Cu/HAP catalyst demonstrates catalytic performance on par with other metal oxide-based catalysts, indicating that HAP-based catalysts warrant further investigation for photothermal CO_2 reduction[133]. The catalytic performance of the HAP-based catalysts for CO_2 methanation can be seen in Table 7.

SURFACE ENGINEERING OF HYDROXYAPATITE CATALYSTS

Active metals deposition

The active center affects the reaction rate, selectivity, and stability of a catalytic reaction. Active centers can be introduced to HAP support through several

Table 5. Catalytic performance of HAP-based catalysts for partial oxidation of methane (POM)

Catalyst	WHSV (ml_{CH4}/gcat.h)	T (°C)	Pressure (bar)	Feed composition	CH_4 conversion (%)	CO selectivity (%)	Stability (mins)	Reference
Ca90NiP(25)	4,800	800	1	$P(CH_4)$ = 16.2 kPa $P(O_2)$ = 8.1 kPa	~95.0	~95.0	n.r.	[102]
	Remarks: The hysteresis in CH_4 conversion can be attributed to CH_4 activation by Ni^0 as the temperature increases. But more of the Ni^0 species become oxidized into NiO by O_2 when temperature decreases. The NiO can still be partially reduced by reactant gas into a mixture of Ni^0 and NiO which makes the catalyst more difficult to reduce but more catalytically stable. The spent Ni-Ca-HAP exposed to ambient air could be reactivated under standard reaction conditions							
HAP(1.61)	3,000	600	1	$P(CH_4)$ = 29.0 kPa $P(O_2)$ = 4.0 kPa	~6.0	n.r.	180	[103]
	Remarks: The formation of PO_4^{3-} ions on the non-stoichiometric HAP surface appears to be favorable to the formation of CO due to enhanced CH_4 activation. As the Ca/P ratio decreases, higher formaldehyde formation was observed							
SrHAP	3,600	600	1	$P(CH_4)$ = 28.7 KPa $P(O_2)$ = 12.3 kPa	~10	~90.0	5,050	[104]
	Remarks: The SrHAP attained high selectivity toward CO formation in the initial 6 h but the CH_4 decreased beyond that. The reason for the decrease in catalytic activity is due to the formation of $Sr_3(PO_4)_2$ which is inactive towards methane formation							
Pb12HAP	3,600	600	1	$P(CH_4)$ = 28.7 kPa $P(O_2)$ = 4.3 kPa	~11.0	~30.0	180	[105]
	Remarks: The partial Pb substitution into the HAP lattice was observed to be beneficial for CH_4 activation. The addition of tetrachloromethane (TCM) could chlorinate the surface and cause catalyst deactivation. However, the CH_3Cl formation was also observed							
BaHAP	3,600	700	1	$P(CH_4)$ = 28.7 kPa $P(O_2)$ = 4.1 kPa	~8.0	~10.0	6	[106]
	Remarks: Ba addition was found to have beneficial effects on CH_4 conversion for POM in the absence of TCM. The introduction of TCM can be beneficial for C_2 selectivity but detrimental to catalyst stability. Methyl chloride formation was also observed							
HAP	3,600	700	1	$P(CH_4)$ = 28.7 kPa $P(O_2)$ = 4.1 kPa	~4.0	~10.0	6	[107]
	Remarks: CH_4 conversion and C_2 selectivity do not significantly change with Ca/P ratio and time. The introduction of N_2O and on-stream TCM can be detrimental to CH_4 conversion and C_2 selectivity							
Ni-Sr-HAP	6,000	750	1	$P(CH_4)$ = 16.1 kPa $P(O_2)$ = 8.2 kPa	~90.0	~90.0	n.r.	[108]
	Remarks: Although the catalyst subjected to the shortest calcination time of 2 h took a lower temperature to activate CH_4 molecules, the CH_4 conversion for the other two catalysts at different calcination times is very similar beyond ~780°C. Longer calcination time creates more $Sr_{3-x}Ni_x(PO_4)_2$ less reducible phase							
Ca95NiP(25)	4,800	750	1	$P(CH_4)$ = 16.1 kPa $P(O_2)$ = 8.2 kPa	~80.0	~88.0	84	[109]
	Remarks: The CaNiP catalysts were prepared by the coprecipitation method and the Ca/PO_4 ratio was found to be optimal for CH_4 conversion at 10/6 due to the presence of surface basic sites and reducible Ni sites for CH_4 activation							
$Ce_{0.1}Ni_{2.5}Ca_{10}$	32,000	600	1	$P(CH_4)$ = 16.1 kPa $P(O_2)$ = 8.1 kPa	~65.0	~60.0	20	[110]

	Remarks: Ce, added as a promoter after the coprecipitation was completed, could enhance CH_4 conversion and improve catalyst stability as Ce can provide oxygen vacancies to promote carbon gasification and so reduce carbon formation							
Ni-Ca-HAP	n.r.	750	1	$P(CH_4)$ = 16.2 kPa $P(O_2)$ = 8.1 kPa	~90.0	~85.0	n.r.	[111]
	Remarks: The Ni-Ca-HAP catalyst was subjected to N_2O pulse chemisorption. The adsorbed CH_4 is converted into CO_2 due to lattice oxygen on the HAP surface. When lattice oxygen depletes, CO formation and, subsequently, carbon formation become more favored. Partially oxidized Ni species are required for high CH_4 conversion and stable performance. The catalyst was deposited onto monolith walls, and it was found that at higher temperatures, the temperature change decreases due to higher heat loss at the reactor walls							
Rh(1)-HAP	19,200	700	1	$P(CH_4)$ = 10.1 kPa $P(O_2)$ = 5.1 kPa	~76.0	~85.0	n.r.	[112]
	Remarks: Three Rh species were observed on the HAP surface from characterization techniques: surface Rh particles, RhOx with good interaction with the support, and Rh incorporated into the HAP lattice structure. Although the dispersion of Rh (1)-HAP appears relatively low, the catalyst stability remains well-preserved over 30 h due to better metal-support interaction which makes it difficult to sinter and oxidize. Rh (1)-HAP catalyst appears comparable to industrial Rh-Al_2O_3 catalyst in CH_4 conversion and H_2 yield							

WHSV: Weight hourly space velocity; n.r.: not reported.

methods, with incipient wetness impregnation as the commonly used strategy. Alternatively, electrostatic adsorption using ammonia can create dispersed active sites on the HAP surface. Additionally, coprecipitation and ion-exchange methods can enhance surface basicity and create dispersed active sites on the HAP catalyst surface[16].

The wetness impregnation method not only deposits the active center onto the catalyst surface but also may perform partial cation exchange as the cations in the impregnation solution may swap with the Ca^{2+} cation during the impregnation process[137]. This creates two different sites with different sizes: one with nanoparticles and the second one with cluster or single atom size. The active center of two different sizes may affect product selectivity. Domínguez *et al.* used HAP as catalyst support, impregnated with Au, for CO oxidation. This catalyst has demonstrated near complete CO conversion at room temperature due to the presence of structural defects by eliminating surface carbonates which alter the Au oxidation state[119]. Wang *et al.* reported that the Au/HAP catalyst calcined under reaction conditions is more active than in air[138]. Higher Au loading resulted in lower CO activity. Further characterization using X-ray photoelectron spectroscopy (XPS) revealed that higher HAP crystallinity resulted in a lower Au^{3+}/Au^0 ratio due to lower Ca/P. This indicates that the surface becomes more acidic, thereby withdrawing more electrons from the Au species and creating Au^{3+}. Further investigation by Huang *et al.* has shown that the calcination temperature and calcination environment can influence CO oxidation activity and selectivity at room temperature due to the formation of very small Au nanoparticles[118]. Although very small Au nanoparticles, thought to contribute to high initial activity, have been observed in TEM images, SMSI is believed to underlie this influence. Tang *et al.*, through an *in-situ* Diffuse reflectance infrared Fourier transform spectroscopy (DRIFTS) study of catalyst samples prepared at different temperatures, have indeed shown that the SMSI effect has a detrimental effect on CO oxidation activity at high calcination temperature as the active sites were encapsulated by HAP support under an oxidative environment[120]. However, such SMSI effect can be tuned and manipulated through partial encapsulation to prevent metal sintering and yet allow selective and adequate catalytic activity to occur on the active sites. In one such demonstration, Fe was introduced into the HAP lattice through cation substitution using the coprecipitation method; the Fe-HAP surface with abundant

Table 6. Catalytic performance of HAP-based catalysts for CO oxidation

Catalyst	WHSV (mL/gcat.h)	$T_{50\%}$ (°C)	Pressure (bar)	Feed composition	Stability (h)	Reference
Au/FH-400	20,000	~-25	1	1.0 mol%CO 1.0 mol%O_2 98 mol%He	300	[117]
	Remarks: The addition of FeO_x, together with increasing calcination temperature, creates strong metal-support interaction for a very stable catalytic performance of 300 h					
Au/HAP-O_2	100,000	14	1	1 mol%CO 20 mol%O_2 79 mol%He	24	[118]
	Remarks: The calcination atmosphere of the Au/HAP catalyst influences the catalytic activity and stability. Although calcination in the He atmosphere produces very fine Au nanoparticles, the rate of deactivation is also the sharpest. However, the one calcined in the O_2 atmosphere exhibits high catalytic activity over 24 h. Strong metal-support interaction between Au and HAP support was proposed to be the main reason					
Au/HAP	31,500	35	1	3.4 mol%CO 21 mol%O_2 75.6 mol%He	n.r.	[119]
	Remarks: The HAP pre-treatment temperature influences CO conversion with nearly 100% conversion at room temperature for the one calcined at 300 °C. The interaction between CO and the HAP support creates structural vacancies that enhance catalytic activity					
Au/HAP(400)	20,000	~0	1	1.0 mol%CO 1.0 mol%O_2 98 mol%He	n.r.	[120]
	Remarks: The strong metal-support interaction (SMSI) effect observed in Au/HAP is reversible, except that it occurs in oxidative conditions. This is the opposite of classical SMSI. SMSI effect helps to make the Au nanoparticle more sintering resistant					
Au-FH(400)-17.5%	20,000	~-30	1	1.0 mol%CO 1.0 mol%O_2 98 mol%He	n.r.	[121]
	Remarks: The presence of FeOx helps to reduce carbonate, an inactive reaction intermediate species, accumulation which helps to enhance catalytic activity					
Au-Cu-HAP	10,890	~30	1	10 mol%CO 90 mol%air	14	[122]
	Remarks: The addition of Au created more O_2 adsorption sites and increased Cu dispersion on the HAP support. The higher Cu dispersion appears to tune the Cu valence between +1 and +2. The latter effect enables the catalyst to be active and stable as compared to a monometallic Cu-HAP catalyst					
Cu(4)-HAP	80,000	~175	1	1.0 mol%CO 1.0 mol%O_2 98 mol%He	n.r.	[123]
	Remarks: The Cu-HAP catalysts with lower loading (0.8% and 3.6%) exhibited better catalytic performance. The Cu lattice micro-strain correspondingly increases with Cu loading and appears to contribute catalytic activity for CO oxidation					

WHSV: Weight hourly space velocity; n.r.: not reported.

OH^- groups and/or PO_4^{2-} groups was speculated to anchor the Au nanoparticles, akin to dispersing Au on FeO_x[139,140]. Consequently, the Au/Fe-HAP (Au/FH) catalyst is significantly more active and stable than that of the conventional Au/Fe_2O_3 (Au/F) catalyst, as shown in Figure 3A[117].

Bimetallic nanoparticles on the catalyst surface often induce two catalytic phenomena: electronic and geometric effects[141]. Guo *et al.* synthesized Au-Cu/HAP for CO oxidation and observed that Cu addition causes a reduction of Au nanoparticle size which resulted in greater Au dispersion. XPS characterization indicated the presence of Cu^+ and Cu^{2+} which appeared to indicate strong interaction with Au[122]. Further characterization using O_2-TPD shows that more oxygen sites are present in the Au-Cu system as compared to the monometallic Au catalytic system[122]. Other than Au, Cu has been used as an active metal for CO oxidation. Different Cu loadings had been impregnated onto stoichiometric HAP for CO oxidation and preferential CO oxidation. The lowest Cu loading at 0.8%wt Cu shows the highest catalytic activity among the other catalyst samples. Surface characterization using XPS and H_2-TPR revealed the presence of Cu^+ species and Cu^{2+} species that might be integrated into the HAP framework. Higher Cu dispersion on the lowest loading catalyst resulted in better CO chemisorption[123].

A noble metal component, such as Pd, has been used for full methane oxidation. In the presence of strong metal-support interaction - induced by increasing the calcination temperature, the Pd coordination changes from tetrahedral to square planar geometry while containing a mixture of Pd^0 and Pd^{2+}[142]. Stronger metal-support interaction can help stabilize the Pd nanoparticles in successive oxidation cycles and provide better catalytic conversion via improvement in PdO reduction[142]. Nickel has been added as a bimetallic component to enhance the catalytic performance but the monometallic nickel displays reasonable performance for full methane oxidation without carbon formation[143].

The presence of Pb appears to increase the ethylene selectivity, which transforms POM into OCM. Other than lead (Pb), barium (Ba) is also used as an active component for the POM reaction. The addition of Ba produces better methane conversion than Ca or Pb, and the resulting trend is similar to what is reported[106].

This property can be utilized to load transition metals, such as Ni, Co, *etc.*, with strong interaction with the HAP support. Depending on the metal loading, the distribution of various types of transition metal species interacting with different support sites is obtained in HAP-based catalysts. For example, in a study by Boukha *et al.*[93], the Ni loading on HAP catalysts varied from 1% to 10% and it was observed that Ni was mostly present as Ni^{2+} ions by ion exchange with Ca^{2+} at lower Ni loadings (< 1 wt%). The progressive increase of Ni loading from 1% to 10% led to the formation of small NiO nanoparticles at less than 2%-4% loading and large NiO nanoparticles at higher loadings. The strong interaction of the metal with the support is highly desirable for DRM to prevent metal sintering at the high reaction temperature and subsequent formation of coke catalyzed by large metal ensembles[144,145]. However, while the ion-exchanged Ni^{2+} has a very strong interaction with HAP support, they exhibited low activity for DRM (as evidenced by poor conversion on the 1% Ni loading catalysts). Thus, the Ni/HAP catalyst with an intermediate Ni loading of 4% and small NiO nanoparticles showed the best performance. The poor activity of the ion-exchanged Ni species may be caused by the cationic state of Ni. Metallic Ni has traditionally been recognized as the active site for DRM, which is why a pre-reduction step before the reaction increases catalytic effectiveness activity. Ion-exchanged Ni^{2+} on HAP is difficult to reduce, possibly leading to lower activity than NiO nanoparticles on HAP, as also reported by other studies[91,94]. Rêgo De Vasconcelos *et al.* compared three loading techniques - ion exchange, incipient wet impregnation, and liquid phase impregnation for Pt and Ru on HAP support and also observed that incipient wetness impregnation resulted in better catalytic performance in DRM[95]. This broadly agrees with the higher activity of smaller metal nanoparticles on HAP

Table 7. Catalytic performance of HAP-based catalysts for CO_2 hydrogenation to CH_4

Catalyst	WHSV (mL/gcat.h)	T (°C)	Pressure (bar)	Feed composition	CO_2 conversion (%)	CH_4 selectivity (%)	Stability (h)	Reference
NiHAP (0.5)	30,000	350	1	8 mol%CO_2 32 mol%H_2 60 mol%He	75-80	97.0	70	[134]
	Remarks: The addition of oleic acid was found to influence the chemical state of Ni which can affect the amount of surface formate on the catalyst surface. A higher amount of Ni^0 is important for methane formation as CO desorbs easily from partially reduced Ni sites							
Ni/La-(6.6)	30,000	350	1	16 mol%CO_2 64 mol%H_2 20 mol%He	70	98.0	100	[135]
	Remarks: La acts as a dual-function material: the first purpose is to chemisorb CO_2 while the second purpose is to create highly dispersed Ni nanoparticles supported on HAP. The presence of such nanoparticles provides active sites for active and stable catalytic CO_2 methanation							
$10Ni_6CeHA$	12,000	325	1	8 mol%CO_2 32 mol%H_2 60 mol%He	92.5	100	n.r.	[136]
	Remarks: Ce was added onto the Ni/HAP catalyst surface and increased the catalytic activity and methane selectivity. The improved catalytic performance can be attributed to increased oxygen vacancy and higher dispersion of the Ni nanoparticles							

WHSV: Weight hourly space velocity; n.r.: stands for not reported.

support with intermediate metal-support interaction than strongly interacting ion-exchanged cationic metal species or weakly interacting larger metal nanoparticles. Similar results were also reported for Pd loaded on HAP in DRM[146].

To further increase methane conversion for POM, Ni was used as an active metal and the CH_4 conversion for Ni-HAP catalyst was comparable to hydrotalcite catalyst as aforementioned[102]. Upon increasing reaction temperature, NiO nanoparticles on the HAP surface were partially externally reduced to Ni^0 in the presence of reductive gases (i.e., H_2, CO, CH_4), along with Ni exsolution from the HAP structure [Figure 3B]. Upon cooling, the catalyst surface reoxidizes, forming a layer of NiO, and the exsolved Ni remains exsolved. When heated again, it returns to the reduced state, allowing for repeated cycles of temperature changes [Figure 3C]. The interesting catalytic performance is attributed to SMSI, where HAP support decorates Ni nanoparticles, enhancing their sintering resistance. During the reaction, larger nickel nanoparticles oxidize, while smaller ones maintain their metallic character. Fresh samples do not show nickel nanoparticles, but they appear post-reaction, suggesting that smaller nanoparticles are key for CH_4 activation and H_2 production[102]. In another example, Ni nanoparticles are deposited onto HAP support using oleic acid. Through the use of *in-situ* DRIFTS and *ex-situ* XANES, the amount of surface formate species is related to the chemical nature of Ni on the catalyst surface, as seen in Figure 3D[134]. A reaction mechanism for the CO_2 methanation was proposed and validated using non-linear kinetic modeling. Although the use of HAP-based material can bring about improvement in CO_2 conversion and CH_4 selectivity, the use of more basic promoters can bring about even greater improvement in catalytic performance.

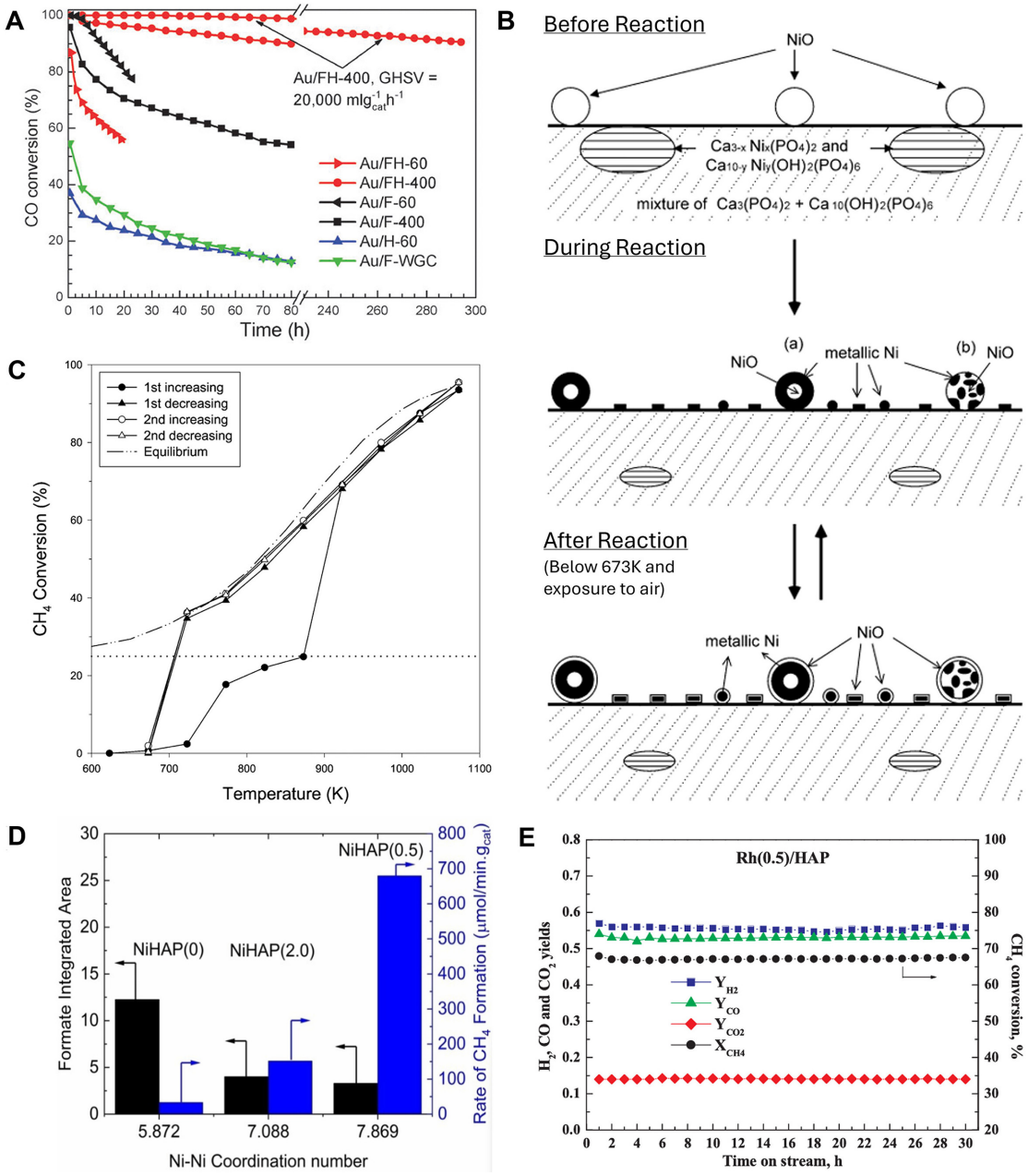

Figure 3. (A) Stability curves in CO oxidation of various catalysts calcined at 400 °C or dried at 60 °C. CO:O_2:He = 1:1:98, GHSV = 200,000 mL/g_{cat}·h for Au/F-60 and Au/FH-60 and 40,000 mL/g_{cat}·h for the others to avoid 100% CO conversion. Reproduced from Ref.[117] with permission from the Royal Society of Chemistry. (B) Proposed scheme of changes of Ni state in partial oxidation of methane (POM) reaction. Reproduced with permission from Ref.[102] with permission from Elsevier. (C) CH_4 conversion for Ca90NiP (20) catalyst was tested two times under increasing and decreasing temperatures. Reproduced from Ref.[102] with permission from Elsevier. (D) HAP structure and influence of Ni-Ni coordination number on formate integrated area at 350 °C and CH_4 formation. Adapted from Ref.[134] with permission from Wiley-VCH GmbH. (E) Activity and product distribution over reduced Rh (0.5)/HAP *vs.* time on stream in the POM reaction. Reaction conditions: 19,000 mL CH_4/g_{cat}·h, m_{cat} = 0.25 g, T = 973 K. Feed composition: 10%CH_4 /5%O_2/N_2. Reproduced from Ref.[112] with permission from Elsevier.

Noble metals such as Rh were also used as active metals for the POM. Three different types of Rh species were observed from H_2-TPR: Rh_2O_3 on the HAP catalyst surface and small RhO_x particles with SMSI and Rh^{2+} cations integrated into the HAP framework. The metal-support interaction of the active metal

component determines the number of metallic sites available for POM; thus, optimum metal-support interaction is required for good methane activation and catalytic stability. Furthermore, the Rh/HAP catalyst at low Rh metal loadings (i.e., 1 wt.%) gave comparable performance to Rh/Al_2O_3 catalyst due to the abundance of basic hydroxyl sites and higher pore size, as shown in Figure 3E[112]. In summary, active metal deposition, the resulting metal-support interactions, and the dispersion state of metal species on HAP significantly influence catalytic performance, product selectivity, and stability across various catalytic conversion reactions.

Cationic substituted catalysts

The substitution of the Ca cations with different cations can affect catalytic activity, product selectivity, and catalyst stability for a myriad of catalytic reactions. The active sites in cation-substituted HAP are more sintering-resistant, as these active sites have better metal-support interaction as compared to the catalyst prepared by the conventional incipient impregnation method[90]. The free metal oxide nanoparticles on HAP support tend to sinter into larger particles during reduction and catalysis, leading to catalyst deactivation and side products. Substituting a transition metal into the HAP lattice improves active site dispersion, reducing side product formation[147]. The partial substitution of the Ca cations has been demonstrated for PDH. Partial cationic substitution using Co^{2+} has led to greater improvement in propane conversion and propylene selectivity as compared to Sr^{3+} and Ba^{2+}. The partial Co substitution in the cation site altered the surface property by making OH^- groups more amenable to hydrogen abstraction from propane, thus creating O^- species[66].

Alternatively, chromium (Cr) can be cation-substituted into the HAP framework via the ion-exchange method and has shown interesting catalytic activity for oxidative propane dehydrogenation. The Cr species changed to Cr^{6+} after air calcination due to oxidation. However, the initial high catalytic activity decreases over time due to the reduction of Cr^{6+} species to Cr^{4+}[67]. However, as chromium can be carcinogenic, other active metals can be explored as an alternative to chromium-based HAP catalysts for oxidative propane dehydrogenation.

CO_2 reduction via the photothermal route has attracted attention for utilizing sunlight to drive catalytic reactions. Photons generate electron-hole pairs or high-energy carriers through localized surface plasmon resonance, which can also induce local heating and enhance catalytic activity through thermal effects[148]. Guo *et al.* have exploited the ability of HAP for partial cation substitution to create highly dispersed Cu species on the HAP surface for photothermal CO_2 reduction to CO by using the coprecipitation method for catalyst synthesis[133]. The activation energy of the CO_2 reduction reaction is lowered by 27.5% and CO formation during the photothermal reaction appears to be dependent on the Cu loading as observed in Figure 4A and B. The effectiveness of the photothermal approach can be attributed to the presence of photogenerated electrons and holes that could be trapped at the Lewis-acidic Cu^{2+} and Lewis-basic PO^{3-}_4 sites of surface frustrated Lewis pair (SFLPs) upon absorption of solar light. This consequently lowered the activation barrier of the CO_2 reduction reaction[149].

Trivalent La^{3+} has been successfully incorporated into HAP up to 7 wt.% due to the close similarity in ionic radius between La^{3+} and Ca^{2+} (i.e., 101 and 100 Å, respectively)[150]. Subsequently, Ni was impregnated, and the HAP with La^{3+}-substitution was found to exhibit better activity in DRM [Figure 4C]. In addition, La promotes carbon nanotube formation instead of parasitic amorphous carbon coating to ensure nickel active sites are able to interact with the reactants and prolonged catalytic lifetime, as illustrated in Figure 4D.

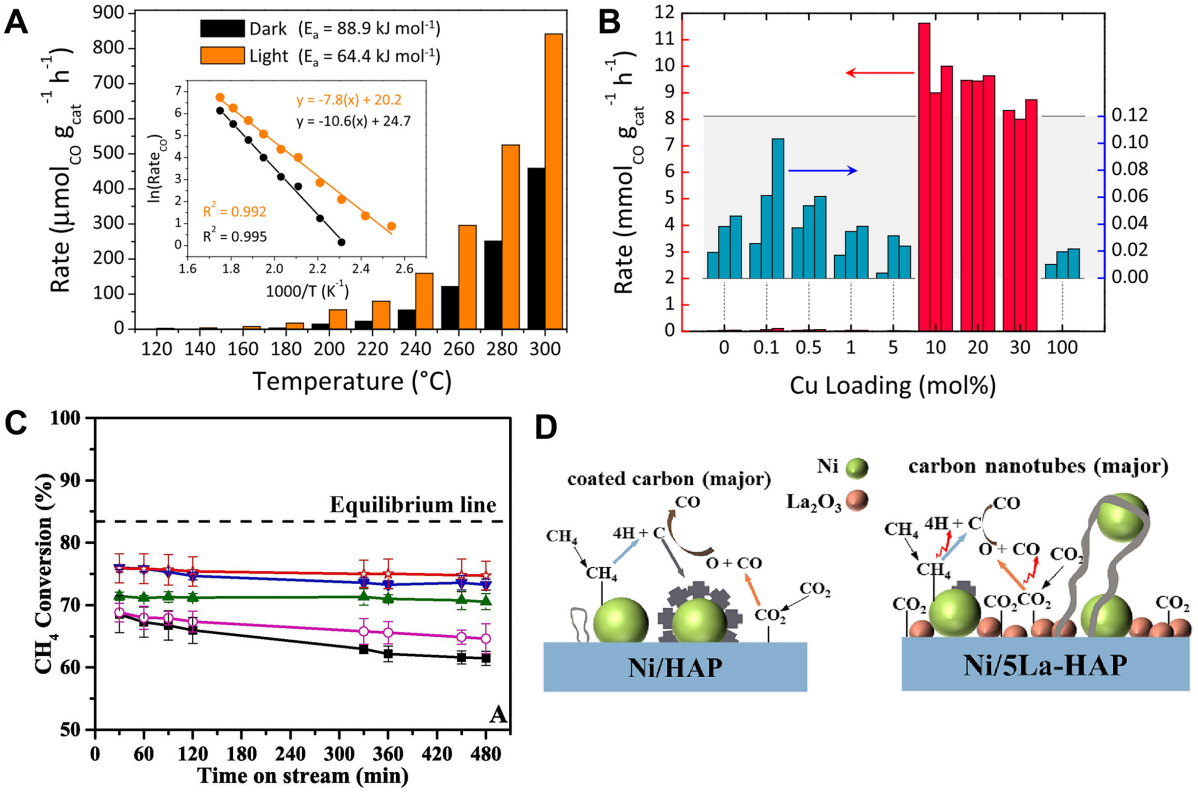

Figure 4. (A) Capillary flow reactor results for the calcined 10 mol% Cu-HAP catalyst. The conversion rates and activation energies, recorded under dark and light conditions, for the selective hydrogenation of CO_2 to CO are plotted. Reproduced from Ref.[133] with permission from American Chemical Society. (B) Photocatalytic reverse-WGS activity of calcined Cu-HAP samples as a function of Cu content in a batch reactor. Reaction conditions: H_2/CO_2 ratio = 1:1, light intensity = 40 suns, no external heating, and measurement time = 1 h. Reproduced from Ref.[133] with permission from American Chemical Society. (C) CH_4 conversion for Ni/xLa-HAP catalysts. Reaction condition: CH_4:CO_2 = 1:1, catalyst weight = 100 mg, total flow rate = 40 mL/min, reaction temperature = 750 °C, GHSV = 24,000 mL/g·h. Adapted from Ref.[150] with permission from Elsevier. (D) Schematic of possible reaction pathways in DRM for La-substituted and pristine Ni/HAP. Adapted from Ref.[150] with permission from Elsevier.

Anionic substituted catalysts

The HAP surface property can be tuned via anion substitution at the B-site by substituting the phosphate group (PO_4) with the vanadate group (VO_4). Calcium vanadate apatite [$Ca_{10}(PO_4)_{6-x}(VO_4)_x(OH)_2$)] was first prepared using coprecipitation of calcium and vanadate aqueous solution with ammonium phosphate dibasic for oxidative PDH[68].

The addition of vanadium to the HAP catalyst induces the formation of lattice oxygen during the reaction due to the structure of the vanadate group. Sugiyama *et al.* reported that the presence of a surface hydroxyl group is beneficial for propane conversion as compared to one without a surface hydroxyl group and that was observed on a partially substituted vanadate HAP catalyst[68]. Partial substitution of the phosphate group with the vanadate group enables the presence of a surface hydroxyl group which maintains the acid-base properties and enables propane activation[68]. Lattice oxygen abstraction creates a redox cycle whereby the vanadium valence charge is reduced from V^{+5} to V^{+4}[151]. This redox behavior is an important characteristic of the oxidative dehydrogenation of propane to propene. Recently, Petit *et al.* have tried to explain this phenomenon by employing *in-situ* DRIFTS and *operando* ionic conductance characterization comprehensively[69]. The partial substitution of the vanadate group into the phosphate group creates more defects and results in fewer OH groups. This causes charge balance on the HAP surface, which results in the

creation of O^{2-} species on the surface at a high temperature (723 K) that was shown to be active in propane activation and conversion to propene, as shown in the proposed mechanism in Figure 5A. Hydroxyl groups in the channels may play a part in activating propane molecules through the creation of O^{2-} groups. The anion exchange between the PO_4^{3-} and CO_3^{2-} anions may also occur through the ball-milling method, which can increase oxygen vacancy concentration on the PO_4^{3-} site[152].

The HAP framework is also flexible towards chlorine storage via anion exchange with the surface hydroxyl groups, also known as A-site substitution, to form chlorapatite. The introduction of chlorine into the HAP framework can be done using tetrachloromethane (TCM). Pre-treatment of the Sr-HAP catalyst with TCM causes the formation of $SrCl_2$ and better ethylene yield can be observed as complete transformation to $Sr_3(PO_4)_2$, an inactive phase, is hindered[105].

Combining cationic and anionic substitution can be done with HAP. Oh *et al.* exploited the tunable nature of the cationic and anionic sites in the HAP framework by using the Pb^{2+} cation and CO_3^{2-} anion to form Pb-HAP-CO_3[58]. The product selectivity and CH_4 conversion were tuned as described in Figure 5B as Pb^{2+} ions can stabilize methyl radicals and facilitate the coupling of methyl radicals to form C_2 by forming covalent bonds with carbon[59]. The presence of the CO_3^{2-} group appeared to maintain the HAP structure under harsh OCM conditions. However, the role of the CO_3^{2-} group in stabilizing the HAP structure remains unclear. As different crystal facets can affect the catalytic activity and product selectivity, Oh *et al.* synthesized two types of HAP catalyst support: one with basal-faceted plane c-surface and prism-faceted a-surface as shown in Figure 5C(i-ii)[60]. The HAP and Pb-HAP with a c-surface performed better than the ones with the a-surface as oxide vacancies and OH^- vacancies found on the c-surface facilitate the formation of methyl or methylene group, which are important to ethylene or ethane from the radical coupling [Figure 5C(iii)]. Thus, there is room for improvement in catalytic activity through a better understanding of the structure-activity relationship of the HAP catalyst through *operando* or *in-situ* characterization of the HAP surface structure.

Use of promoters in HAP catalysts

Alkali, alkaline earth, and noble metal promoters are frequently used in heterogeneous catalysis for positive benefits in catalytic activity and selectivity. In general, there are two types of promoters: structural and textural. Structural promoters enhance the desired product selectivity for a certain reaction by making the desired reaction pathway more energetically favorable[153]. Textural promoters attenuate catalyst nanoparticle agglomeration due to metal sintering; thereby, increasing catalytic stability[154,155].

In several reports on CO oxidation, the active site is frequently poisoned by the formation of carbonate, which leads to reduced catalytic activity. Basic elements such as Na can be added to the catalyst to decrease the number of basic sites, enabling better desorption of CO_2 and resulting in less poisoning of the active sites[156]. Noble metal promoters are used for CO oxidation. Other than Au, Ag is also used as a cheaper alternative for CO oxidation in recent years. Silver doping in the HAP framework produced stable and active CO oxidation catalyst at high temperatures. The silver-doped HAP catalyst also demonstrated stable catalytic performance despite multiple cycles. However, the silver-doped HAP catalyst shows favorable room for improvement[157].

For the WGS reaction, the increase in surface basicity by the addition of alkaline earth or basic elements such as Sr, Na, and K helps to strengthen CO adsorption and favors water dissociation[158-160]. Iriarte *et al.* used calcined pork bone with HAP as the main phase and a minute amount of potassium as the support to be impregnated with Ni, Co, Cu and Fe[161]. The Ni-impregnated catalyst is found to be more active and selective to H_2 formation than the other catalyst due to the presence of trace amounts of potassium, which

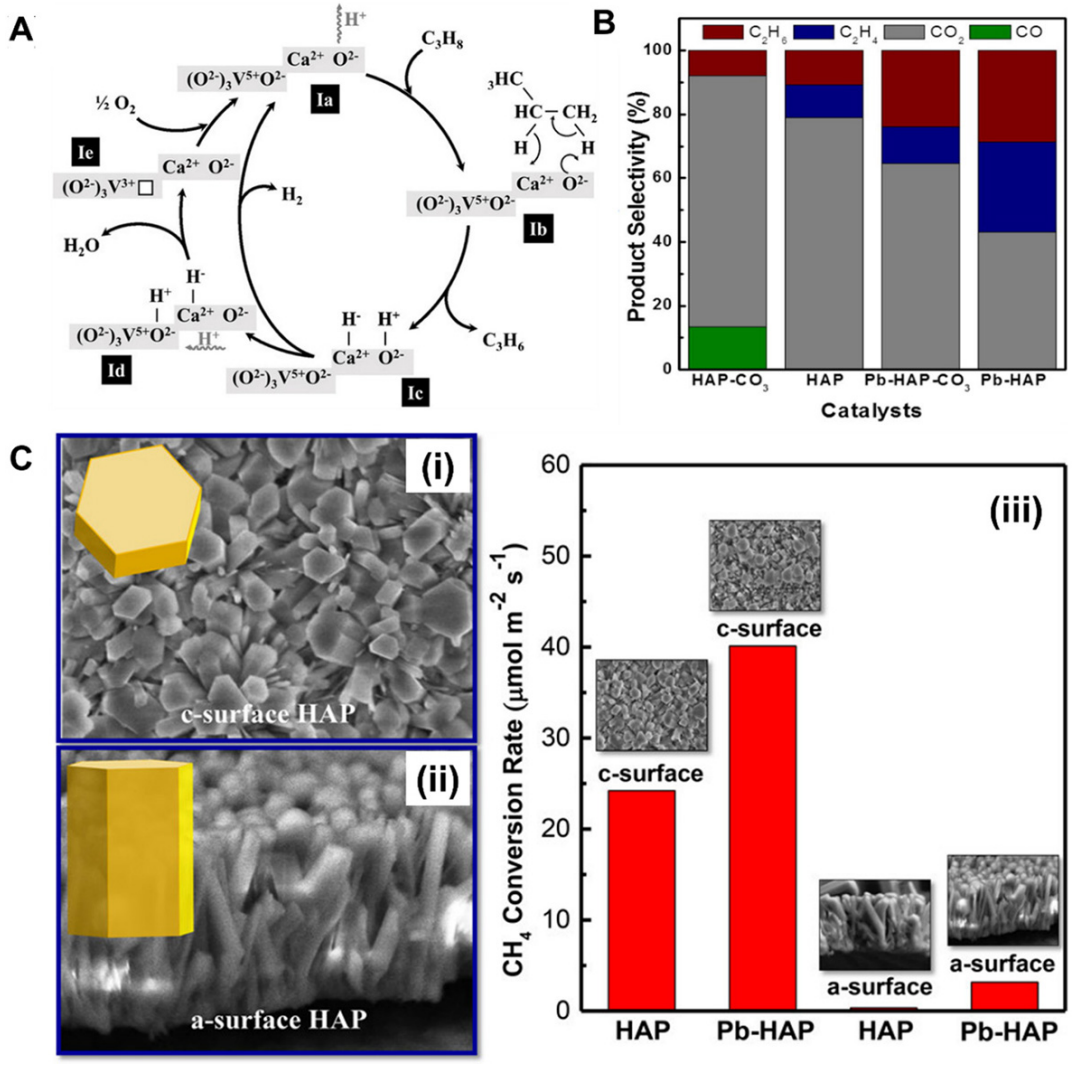

Figure 5. (A) Schematized representation of the catalytic transformation of propane to propylene via non-oxidative and oxidative dehydrogenation routes on V-HAP samples with Ca^{2+}-O^{2-} surface acid-base pairs generated due to proton migration process close to VO_4 tetrahedra. The square box represents oxygen vacancy and the squiggly arrow refers to the proton migration process. Reproduced from Ref.[69] with permission from Wiley-VCH GmbH. (B) Product selectivity for OCM reactions over HAP-based catalysts at 23% conversion under 973 K and 101 kPa pressure conditions and a space velocity of 8,800 mL·gcat^{-1}·h^{-1}. Reproduced from Ref.[58] with permission from Elsevier. (C) c-surface HAP (i), a-surface HAP (ii), the CH_4 conversion rate of the Pb-HAP catalyst with different orientations for OCM reaction. Reproduced from Ref.[60] with permission from American Chemical Society.

suppresses methane formation. K is postulated to block the active site for CO methanation reaction. This study shows that a minute amount of alkaline promoter in naturally sourced material such as bones can be beneficial towards WGS reaction. It also highlights bones as a rich and accessible source of HAP when properly treated.

The addition of Lanthanum Oxide (La_2O_3) as a promoter has been explored in HAP. The increased La loading at fixed Ni loading enables higher CO_2 conversion and CH_4 selectivity in CO_2 methanation, as shown in Figure 6A and B[135]. The increased addition of La_2O_3 introduces strong basic sites at greater concentrations, helping to strengthen CO_2 chemisorption to the catalyst surface, which aids in CO_2 conversion and eventual CH_4 formation, as observed in Figure 6C. Additionally, La_2O_3 can enhance the

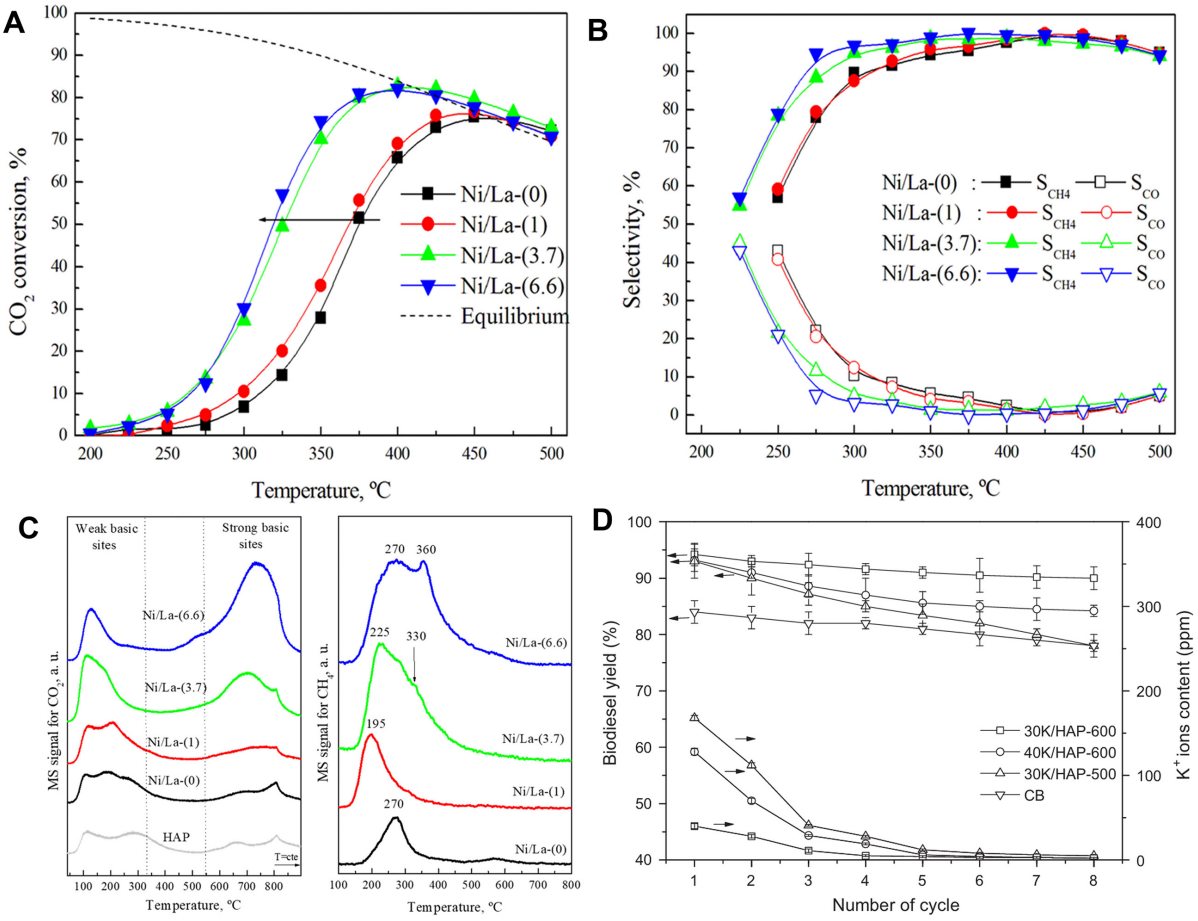

Figure 6. (A) CO_2 conversion and (B) CH_4 selectivity of the Ni/La-(x) catalysts in the CO_2 methanation reaction. Reaction mixture conditions: 16% CO_2 and 64% H_2, balanced in He (WHSV = 30,000 mL/g.h). Reproduced from Ref.[135] with permission from Elsevier. (C) CO_2-TPD (Left) and CH_4 formation during TPSR experiments (Right) with pre-adsorbed CO_2 on the reduced Ni/La-(x) catalysts. Reproduced from Ref.[135] with permission from Elsevier. (D) Reusability studies of catalysts with leaching content of K^+ ions. Reproduced from Ref.[75] with permission from Elsevier.

dispersion of Ni nanoparticles, thereby making the catalyst more reducible. Other metals can also enhance the dispersion of Ni nanoparticles, such as alloying strategy with Co[162] or Ca as a monolayer[163]. In addition, the Co was demonstrated to inhibit graphitic carbon formation in DRM, thereby improving catalytic stability.

Ceria is usually added as a promoter to increase the presence of oxygen species. The presence of oxygen species from Ce helps to alleviate carbon formation by promoting the Bouduoard reaction ($C + CO_2 \rightarrow 2CO$) which will increase CO selectivity[110]. As the presence of oxygen vacancy promotes the CO_2 methanation reaction, ceria was added as a promoter onto Ni/HAP catalyst in a highly dispersed fashion. The resultant catalytic performance was comparable to other metal oxide catalysts which demonstrated the suitability of HAP support for CO_2 methanation. Nguyen *et al.* added ceria to Ni/HAP catalyst for CO_2 methanation and observed enhanced CO_2 conversion and CH_4 selectivity as compared to the undoped sample[136]. The enhancement in catalytic performance can be attributed to higher Ni nanoparticle dispersion and higher Ni reducibility. In addition, the presence of CeO_2 introduces more medium basic sites. The introduction of medium basic sites may originate from the facile redox property of ceria to transit from Ce^{4+} to Ce^{3+} and *vice versa*. The redox property also creates oxygen vacancies which

enhances CO_2 chemisorption. The stronger CO_2 chemisorption leads to the formation of monodentate formate which is beneficial to methane formation and, subsequently, higher methane selectivity[164]. Hence, CeO_2 acts more as a structural promoter in this work.

Other than CO oxidation and WGS reaction, the transesterification reaction requires a highly basic or alkaline element to accelerate the reaction towards FAME formation. To enhance the alkalinity of the HAP catalyst surface, K_2CO_3, Sr, and Li were impregnated onto the bone-derived HAP catalyst support, respectively. The FAME yield increases in the following order: Li/HAP (93.2%) < Sr/HAP (94.7%) < 30K/HAP-600 (96.4%)[75]. The better catalytic performance exhibited by the 30K/HAP-600 catalyst is due to the higher strength of the basic sites and greater concentration of surface basic sites. The FAME yield was found to be not just dependent on the K_2CO_3 loading but also on the calcination temperature. However, if the calcination temperature is too high, the FAME yield is observed to decrease, which may be attributed to K_2CO_3 sintering and lower Brunauer-Emmett-Teller (BET) surface area. The authors also studied the extent of potassium leaching as catalytic stability is an important factor in commercial applications and potassium salt tends to leach during the reaction[165]. The extent of potassium leach was found to be reduced with increasing calcination temperature due to the creation of the $KCaPO_4$ phase that is more active and stable for biodiesel production [Figure 6D]. The Na-doped HAP catalyst can attain high rapeseed oil conversion and high selectivity to FAME, thereby attaining high FAME yield at 99%. The produced biodiesel is comparable to EU biodiesel testing standard EN 14214. Catalyst leaching did not occur due to strong Na^+ integration into the HAP framework. Impregnating the bone-derived HAP catalyst with K can result in a higher FAME yield at 96.1%[166]. Furthermore, the produced biodiesel can satisfy ASTM biodiesel specifications.

Single atom and cluster on HAP catalyst

Single-atom catalysts (SAC) have received extensive research attention due to their promise of high atom efficiency and favorable metal-support interaction[167]. Ion exchange method is most commonly used to synthesize SAC using HAP as catalyst support. The seminal work by Yamaguchi *et al.* used the ion-exchange method to produce single-atom Ru^{3+}, which substitutes Ca^{2+} in the HAP framework[168]. The presence of Ru^{3+} had been evidenced using XANES and EXAFS, as observed in Figure 7A. The Ru^{3+} species are observed to be coordinated to the Cl atom, which produces a highly active catalyst for aerobic alcohol oxidation. The same ion exchange method has been demonstrated for single atomic Pd[143], and Co[169], on HAP. Theoretical and computational study was conducted on single atomic transition metals (i.e., Fe, Co, Ni, and Cu) on HAP, revealing their suitability in direct POM to methanol[170]. The ion-exchange method can also be used to deposit clusters on HAP support as well. Tounsi *et al.* reported that the time taken for ion exchange to occur plays an important role in influencing the nature of Cu species and Cu loading as Cu^{2+} species will first chemisorb onto the HAP surface, followed by a slower reaction to be integrated into the HAP framework[171]. Although Tounsi *et al.* claimed that CuO was present on the HAP, no TEM and XANES characterization were shown to support this claim[171]. Thus, the effect of ion-exchange time on cluster formation requires further investigation. Lu *et al.* performed DFT on Fe-exchanged HAP for oxygen reduction reaction (ORR)[172]. The first principles study indicated that Fe species exchanged at $Ca_{(II)}$ site is more favorable. The Fe species at that site is favorable towards oxygen chemisorption which is the highest energy barrier to overcome to start ORR. The electrostatic adsorption method was used to create highly dispersed Ni-active sites on Ce-doped HAP [Figure 7B], which was characterized by higher activity and stability in DRM[89]. Although active sites in the form of single atoms and clusters can be deposited onto HAP support, the mesoporosity of the HAP support can be increased to enhance active site dispersion.

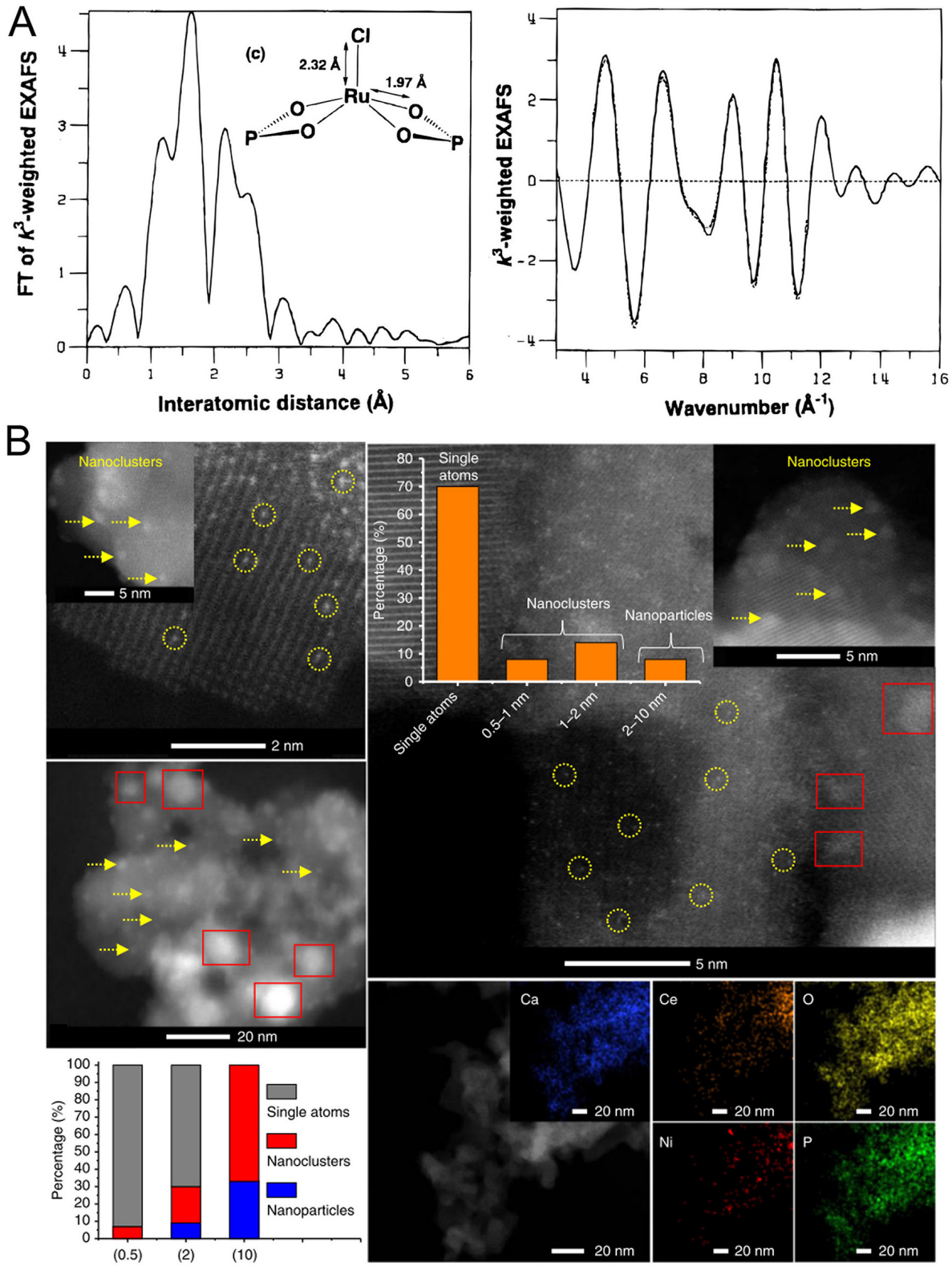

Figure 7. (A) FT magnitude of k^3-weighted EXAFS of RuHAP with an inset showing a proposed surface around Ru^{3+} of the RuHAP catalyst (Left) and inverse FT of the peaks with the 0.8 < R/Å < 2.8 range (Right). Adapted from Ref.[168] with permission from American Chemical Society. (B) Electron microscopy images and size distribution with evidence of single-atom Ni in $0.5Ni_1$/HAP-Ce samples. Adapted from Ref.[89] under CC BY 4.0 license.

Mesoporosity in HAP-based catalyst

The ability to control the catalyst pore size can have a profound effect on product selectivity[173]. The catalyst pore size can be tuned by two methods: soft-template and hard-template. The effect of pore structure in the HAP support on the DRM performance of Ni/HAP catalysts was reported by Li *et al.*[97]. The mesopore/macropore ratio of the support can be altered by adjusting the urea-hydrolysis precipitation temperature. This ratio dictates Ni dispersion and the size and interaction of NiO nanoparticles with the support. A high fraction of macropores results in poor Ni dispersion and low metal-support interaction. As mesopores increase, Ni preferentially disperses along mesopore channel walls, resulting in smaller nanoparticles with enhanced metal-support interaction and improved activity. However, too small pore sizes cause blockage by Ni nanoparticles, leading to suboptimal DRM activity. In another study, the specific surface area and pore structure of the HAP support were modified using various surfactants in a soft-templating synthesis approach. Soft templating by a combination of two surfactants was reported to significantly increase the surface area and enhance reactant conversion in DRM[146]. The use of surfactants such as CTAB during the synthesis stage can help to increase BET surface area. Essamlali *et al.* utilized CTAB to increase the synthetic HAP surface area, in addition, to increasing surface basicity by impregnating with Na[79]. The hard templating method first involves the hydrothermal treatment of SBA-15 in sucrose solution to produce carbonized sucrose in the SBA-15 pores[174]. The SBA-15 SiO_2 hard template was removed by washing with concentrated NaOH to obtain carbon nanorods. Those carbon nanorods were added to the coprecipitation solution for HAP nanoparticle synthesis. The BET surface area of the resultant HAP after air calcination is 242.2 $m^2/g_{cat,}$ which is among the highest BET surface areas reported for the HAP material.

The HAP BET surface area can be increased using various treatment methods. Bone-derived HAP catalyst underwent two preparation methods: (1) hydrothermal treatment after calcination, and (2) without hydrothermal treatment after calcination[175]. The hydrothermal-treated sample showed a higher BET surface area and FAME yield, indicating improved access to active sites due to increased surface area and mesopores, as shown in the BET results. However, no relationship was found between hydrothermal duration and catalytic activity. Ghanei *et al.* used waste bone and reported low catalytic activity[78]. Their procedure indicated an average particle size of 180-300 μm, resulting in a lower BET surface area of 3-5 m^2/g. Therefore, the preparation method and type of bone significantly influence catalytic performance.

FUTURE RESEARCH DIRECTIONS AND OUTLOOK

The HAP unit cell structure accommodates various cations due to similar ionic radii and valence charges. Cations integrate into HAP through surface complexation, which involves liquid-solid mass transfer that can create resistance. Therefore, it is crucial to explore strategies to speed up the substitution. The Ca/P ratio also significantly affects the HAP surface basicity or acidity. For DRM, the presence of basic sites generally helps to alleviate carbon filament formation, thereby extending the longevity of the catalytic performance. For other catalytic reactions such as WGS reaction, higher surface basicity helps with enhancing water dissociation; thereby, higher H_2 formation[160]. To better understand the surfaces of HAP-based catalyst surfaces, *in-situ* or *operando* spectroscopic techniques such as DRIFTS, XPS, and X-ray absorption spectroscopy (XAS) can be used to gain insight into the active metal (e.g., Ni)-Ca coordination, which may be important to understand metal-support interaction.

According to the literature examined in the review manuscript, Ca(II) is observed to be the site of choice for cation substitution. Limited studies attempted to investigate the concentration of Ni^{2+} substituted into the $Ca_{(I)}$ or $Ca_{(II)}$ sites[90]. However, the structure-activity relationship between DRM activity and the concentration of Ni^{2+} substituted into the $Ca_{(I)}$ or $Ca_{(II)}$ remains unclear. Using DFT and microkinetic modeling to clarify the structure-activity relationship for DRM would be interesting, involving examining

how catalytic activity improves with varying Ni^{2+} concentrations in $Ca_{(I)}$ or $Ca_{(II)}$ sites. In fact, DFT studies have been employed in other reaction studies, such as the ORR using Fe-doped HAP, where DFT uncovered superiority in reducing O_2 to H_2O with less kinetic and thermodynamic barrier in the OH hydrogenation or 2OH self-dehydration in Fe-substituted HAP (i.e., Fe@HAP) compared to Fe/HAp[172]. DFT and microkinetic studies were employed to uncover how the unique combination of acidic and basic properties of HAP facilitates different elementary reactions in ethanol-to-butanol biofuels production[176], or how defects in HAP can stabilize intermediate reaction species[177]. Importantly, DFT is not only a tool for understanding cationic substitutability as earlier elucidated[42,43], but can reveal key mechanistic insights not limited to preferential reaction pathways or adsorption affinity on different active sites (i.e., active metals, or defects on HAP)[132,178]. Substitution with foreign anion at either the OH^- group or PO_4^{2-} group can affect surface properties of the HAP surface, especially surface acidity and basicity. Currently, there is a scarcity of literature on HAP-based catalysts examining the effect of anionic substitution on catalytic activity, except for the ones on oxidative PDH and OCM. More experimental studies on the effect of anionic substitution on catalytic activity and product selectivity for CO_2 methanation, WGS reaction, CO oxidation, and DRM can be examined in greater detail. For example, studying how CO_2 can be absorbed in HAP through anionic substitution as carbonated HAP[179,180] or possibly with exsolved calcium ions after cationic substitution may be an interesting avenue of research for identifying efficient, low-cost carbon capture or chemical looping materials[181].

Core-shell nanoarchitectures involving the HAP nanoparticles were primarily used for gas sensors and non-catalytic applications[182-184]. HAP-based catalysts have shown promise in high-temperature reactions such as DRM and OCM. Their catalytic stability can be improved by encapsulating HAP nanoparticles with inert shells (e.g., SiO_2) using methods such as Stöber synthesis or reverse microemulsion. Promoters play a critical role by blocking undesired reaction pathways, enhancing reactant adsorption, and improving product selectivity. Alkaline or basic promoters facilitate water dissociation, aiding WGS reaction rates, and also enhance the reducibility of active metal centers.

In CO_2 capture and utilization, such promoters enable dual-function materials that both adsorb and convert CO_2[185]. During flue gas exposure, CO_2 is captured at basic sites; when switched to H_2, the adsorbed CO_2 is converted into products such as CH_3OH or CH_4 at metal sites. These promoters also increase surface basicity, which improves biodiesel yields. To fully understand their role, it is important to examine whether they also influence catalyst structure and texture, using both *ex-situ* and *in-situ* characterizations on spent catalysts.

Literature reports that the BET surface area of HAP-based catalysts can vary widely, from as low as 5 up to 242.2 m^2/g. The highest values are typically achieved using hard templating methods, such as SBA-15-derived carbon nanorods. However, this approach is complex and time-consuming. Despite the promise of mesoporous HAP, its actual use in catalysis remains limited. Alternatively, poly(methyl methacrylate) (PMMA) can serve as a hard template that burns off easily, potentially saving synthesis time and reducing costs. Although natural bones can still be used as a source of HAP, the BET surface area is still very low (~3-5 m^2/g), which implies that the HAP particles are in the micron range. Thus, in addition to physical pulverization, the size of natural bone-derived HAP may be further reduced using a ball-milling technique. Although increasing the ball-milling speed can result in smaller particle sizes, the phase of the material may change. Therefore, it is important to optimize the ball-milling speed to achieve a minimum particle size without significantly altering the material phase.

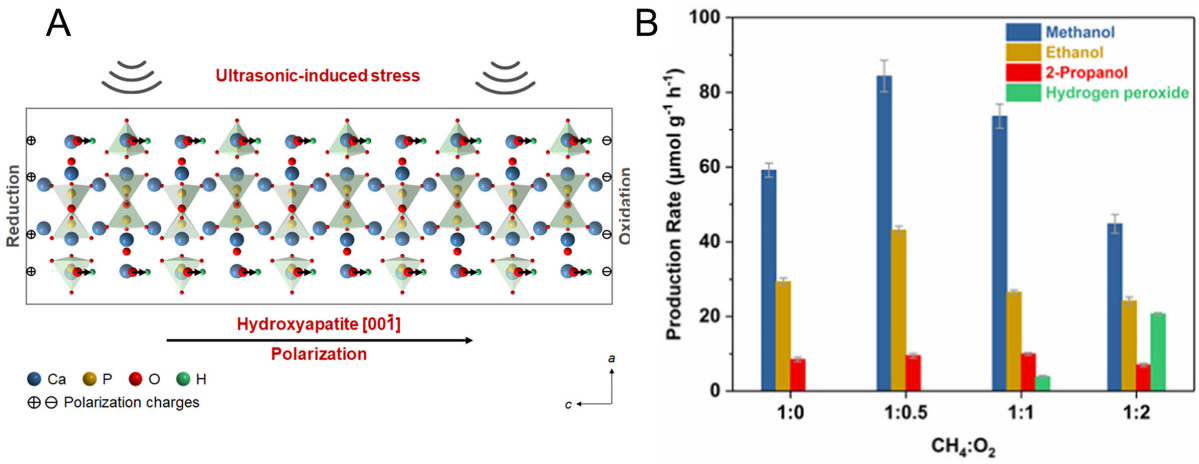

Figure 8. (A) Piezoelectric effect of HAP. Reproduced from Ref.[191] with permission from Elsevier. (B) Alcohol production at different CH_4:O_2 ratios for HAP via piezoelectric catalysis. Reproduced from Ref.[191] with permission from Elsevier.

More recently, piezoelectric catalysis has gained increasing research attention to generate reactive oxygen species (ROS) - hydroxyl radicals (OH·) can activate C-H bond in methane at milder conditions to facilitate C-C coupling to form hydrocarbon compounds and oxygenates[186,187]. Piezoelectric materials, upon application of mechanical stress, can induce the asymmetrical distribution of surface charge and start an electrochemical reaction[188]. HAP is found to possess piezoelectric properties, which can be exploited to generate ROS[189,190]. Zhou *et al.* recently studied the use of HAP as a potential material for piezoelectric methane oxidation[191]. Interestingly, the HAP material, upon ultrasonic-induced stresses, produces hydroxyl radical (•OH) to attack the methane C-H bond and negative surface charges to drive methanol dehydration into methyl carbene as a C1 precursor for upgrading into C_2-C_3 alcohols, as shown in Figure 8. Further examination of the surface engineering strategies discussed in this review on HAP as piezoelectric catalysts could be an interesting future research focus.

We have covered sustainable chemical production via OCM, PDH, biodiesel production, and H_2 production and/or CO_2-modulating reactions, including CO_2-utilizing DRM, POM, CO oxidation, and CO_2 methanation. However, other reactions relevant to sustainable chemical and fuel production include CO_2 hydrogenation to methanol, CO_2 hydrogenation to olefins and aromatics, and the upgrading of alcohol (ethanol) to higher alcohols[192], which can benefit from HAP-based catalysts. However, these are explored only to a limited extent. Additionally, to the best of our knowledge, there seems to be a scarcity of literature regarding the economics of HAP-based catalyst production. According to Guo *et al.*, the cost to produce the copper HAP catalyst is approximately USD 1.0 per kilogram[133]. However, this calculation does not account for key factors such as operating costs and bulk raw material pricing. HAP is often viewed as a green and sustainable catalyst, especially because it can be derived from bio-based waste sources such as animal bones and fish scales. This not only reduces environmental impact but also improves the overall sustainability of HAP-based catalytic systems. That said, the feasibility of scaling up HAP - whether to pilot[193] or commercial levels - still requires further investigation, particularly in terms of supply chain and catalytic performance.

CONCLUSION

The propensity of HAP material for cation and/or anion substitution enhances surface basicity, creates active sites, and introduces lattice oxygen species. As a result, new active sites can be formed for catalytic reactions that are crucial for chemical and fuel products such as DRM, CO_2 hydrogenation, POM, CO

oxidation, and biodiesel production. The basicity of the HAP surface can be adjusted by adding basic and alkaline elements such as K, Na, and Sr. Incorporating these elements helps improve product selectivity and reactant conversion. For certain reactions that rely on precious metals as active sites, metal loading can be reduced by employing single-atom or cluster catalysts. Cationic substitution in HAP can be utilized to generate such single atoms and clusters, which may be catalytically active, selective, and stable for reactions essential to developing more sustainable fuels and chemical products such as CO_2 hydrogenation and DRM. Enhancements in these catalytic properties would lead to higher product yields, thereby lowering manufacturing costs. Improvements in catalytic performance using HAP-based catalysts can be achieved through a deeper understanding of the HAP surface, utilizing synergistic surface characterization techniques such as XAS, XPS, and FTIR in either *in-situ* or *operando* mode.

DECLARATIONS

Authors' contributions

Wrote the manuscript: Lim, K. H.; Wai, M. H.
Reviewed the manuscript: Cao, K.; Das, S.; Nzihou, A.; Kawi, S.

Availability of data and materials

Not applicable.

Financial support and sponsorship

The authors acknowledge the financial support by the National Research Foundation, Singapore, and A*STAR under its Low-Carbon Energy Research (LCER) Funding Initiative (FI) Project (U2102d2011, WBS: A-8000278-00-00).

Conflicts of interest

Kawi, S. is an Editorial Board Member of the journal *Energy Materials* but is not involved in any steps of editorial processing, notably including reviewer selection, manuscript handling, or decision-making, while the other authors have declared that they have no conflicts of interest.

Ethical approval and consent to participate

Not applicable.

Consent for publication

Not applicable.

REFERENCES

1. Lim, K. H.; Yue, Y.; Bella; et al. Sustainable hydrogen and ammonia technologies with nonthermal plasma catalysis: mechanistic insights and technoeconomic analysis. *ACS. Sustain. Chem. Eng.* **2023**, *11*, 4903-33. DOI
2. Julkapli, N. M.; Bagheri, S. Graphene supported heterogeneous catalysts: an overview. *Int. J. Hydrogen. Energy.* **2015**, *40*, 948-79. DOI
3. Liu, X.; Dai, L. Carbon-based metal-free catalysts. *Nat. Rev. Mater.* **2016**, *1*, 201664. DOI
4. Lee, J.; Farha, O. K.; Roberts, J.; Scheidt, K. A.; Nguyen, S. T.; Hupp, J. T. Metal-organic framework materials as catalysts. *Chem. Soc. Rev.* **2009**, *38*, 1450-9. DOI PubMed
5. Jiao, L.; Wang, Y.; Jiang, H. L.; Xu, Q. Metal-organic frameworks as platforms for catalytic applications. *Adv. Mater.* **2018**, *30*, e1703663. DOI
6. Wang, Q.; Astruc, D. State of the art and prospects in metal-organic framework (MOF)-based and MOF-derived nanocatalysis. *Chem. Rev.* **2020**, *120*, 1438-511. DOI PubMed

7. Santos, V. P.; Wezendonk, T. A.; Jaén, J. J.; et al. Metal organic framework-mediated synthesis of highly active and stable Fischer-Tropsch catalysts. *Nat. Commun.* **2015**, *6*, 6451. DOI
8. Frei, M. S.; Mondelli, C.; García-Muelas, R.; et al. Atomic-scale engineering of indium oxide promotion by palladium for methanol production via CO_2 hydrogenation. *Nat. Commun.* **2019**, *10*, 3377. DOI PubMed PMC
9. Wang, J.; Li, W. C.; Sun, D. H.; He, L.; Zhou, B. C.; Lu, A. H. High-selective upgrading of ethanol to C_{4-10} alcohols over hydroxyapatite catalyst with superior basicity. *ACS. Sustain. Chem. Eng.* **2025**, *13*, 36-45. DOI
10. Tsuchida, T.; Sakuma, S.; Takeguchi, T.; Ueda, W. Direct synthesis of *n*-butanol from ethanol over nonstoichiometric hydroxyapatite. *Ind. Eng. Chem. Res.* **2006**, *45*, 8634-42. DOI
11. Qi, H.; Li, Y.; Zhou, Z.; et al. Synthesis of piperidines and pyridine from furfural over a surface single-atom alloy Ru_1Co_{NP} catalyst. *Nat. Commun.* **2023**, *14*, 6329. DOI PubMed PMC
12. Ibrahim, M.; Labaki, M.; Giraudon, J. M.; Lamonier, J. F. Hydroxyapatite, a multifunctional material for air, water and soil pollution control: a review. *J. Hazard. Mater.* **2020**, *383*, 121139. DOI PubMed
13. Kaneda, K.; Mizugaki, T. Development of concerto metal catalysts using apatite compounds for green organic syntheses. *Energy. Environ. Sci.* **2009**, *2*, 655. DOI
14. Fihri, A.; Len, C.; Varma, R. S.; Solhy, A. Hydroxyapatite: a review of syntheses, structure and applications in heterogeneous catalysis. *Coordin. Chem. Rev.* **2017**, *347*, 48-76. DOI
15. Sadat-Shojai, M.; Khorasani, M. T.; Dinpanah-Khoshdargi, E.; Jamshidi, A. Synthesis methods for nanosized hydroxyapatite with diverse structures. *Acta. Biomater.* **2013**, *9*, 7591-621. DOI PubMed
16. Pham Minh, D. Introduction to hydroxyapatite-based materials in heterogeneous catalysis; 2022; pp. 1-18. DOI
17. Mostafa, N. Y.; Brown, P. W. Computer simulation of stoichiometric hydroxyapatite: structure and substitutions. *J. Phys. Chem. Solids.* **2007**, *68*, 431-7. DOI
18. Ammar, M.; Ashraf, S.; Baltrusaitis, J. Nutrient-doped hydroxyapatite: structure, synthesis and properties. *Ceramics* **2023**, *6*, 1799-825. DOI
19. Tsuchida, T.; Kubo, J.; Yoshioka, T.; Sakuma, S.; Takeguchi, T.; Ueda, W. Reaction of ethanol over hydroxyapatite affected by Ca/P ratio of catalyst. *J. Catal.* **2008**, *259*, 183-9. DOI
20. Bailliez, S.; Nzihou, A.; Bèche, E.; Flamant, G. Removal of lead (Pb) by hydroxyapatite sorbent. *Process. Saf. Environ. Prot.* **2004**, *82*, 175-80. DOI
21. Pizzala, H.; Caldarelli, S.; Eon, J. G.; et al. A solid-state NMR study of lead and vanadium substitution into hydroxyapatite. *J. Am. Chem. Soc.* **2009**, *131*, 5145-52. DOI
22. Robles-Águila, M.; Reyes-Avendaño, J.; Mendoza, M. Structural analysis of metal-doped (Mn, Fe, Co, Ni, Cu, Zn) calcium hydroxyapatite synthetized by a sol-gel microwave-assisted method. *Ceram. Int.* **2017**, *43*, 12705-9. DOI
23. Takahashi, H.; Yashima, M.; Kakihana, M.; Yoshimura, M. A differential scanning calorimeter study of the monoclinic ($P2_1/b$)↔ hexagonal ($P6_3/m$) reversible phase transition in hydroxyapatite. *Thermochim. Acta.* **2001**, *371*, 53-6. DOI
24. Ma, G.; Liu, X. Y. Hydroxyapatite: hexagonal or monoclinic? *Cryst. Growth. Des.* **2009**, *9*, 2991-4. DOI
25. Van Rees, H. B.; Mengeot, M.; Kostiner, E. Monoclinic-hexagonal transition in hydroxyapatite and deuterohydroxyapatite single crystals. *Mater. Res. Bull.* **1973**, *8*, 1307-9. DOI
26. Li, W.; Zhang, G.; Jiang, X.; et al. CO_2 hydrogenation on unpromoted and M-promoted Co/TiO_2 catalysts (M = Zr, K, Cs): effects of crystal phase of supports and metal-support interaction on tuning product distribution. *ACS. Catal.* **2019**, *9*, 2739-51. DOI
27. Jiang, F.; Wang, S.; Liu, B.; et al. Insights into the influence of CeO_2 crystal facet on CO_2 hydrogenation to methanol over Pd/CeO_2 catalysts. *ACS. Catal.* **2020**, *10*, 11493-509. DOI
28. Zhao, Z.; Jiang, Q.; Wang, Q.; et al. Effect of rutile content on the catalytic performance of Ru/TiO_2 catalyst for low-temperature CO_2 methanation. *ACS. Sustain. Chem. Eng.* **2021**, *9*, 14288-96. DOI
29. Moteki, T.; Flaherty, D. W. Mechanistic insight to C-C bond formation and predictive models for cascade reactions among alcohols on Ca- and Sr-hydroxyapatites. *ACS. Catal.* **2016**, *6*, 4170-83. DOI
30. Bett, J. A. S.; Christner, L. G.; Hall, W. K. Hydrogen held by solids. XII. Hydroxyapatite catalysts. *J. Am. Chem. Soc.* **1967**, *89*, 5535-41. DOI
31. Wang, Y. B.; He, L.; Zhou, B. C.; et al. Hydroxyapatite nanorods rich in [Ca-O-P] sites stabilized Ni species for methane dry reforming. *Ind. Eng. Chem. Res.* **2021**, *60*, 15064-73. DOI
32. Lin, T.; Liu, C.; Gangarajula, Y.; et al. Strong metal-support interaction induced sintering-resistant Ni nanoparticles supported on highly CO_2-activating vanadium hydroxyapatite for dry reforming of methane. *Appl. Cata. A. Gen.* **2023**, *662*, 119290. DOI
33. Ferri, M.; Campisi, S.; Scavini, M.; Evangelisti, C.; Carniti, P.; Gervasini, A. In-depth study of the mechanism of heavy metal trapping on the surface of hydroxyapatite. *Appl. Surf. Sci.* **2019**, *475*, 397-409. DOI
34. Jemli, Y. E. L.; Abdelouahdi, K.; Minh, D. P.; Barakat, A.; Solhy, A. Synthesis and characterization of hydroxyapatite and hydroxyapatite-based catalysts. In: Pham Minh D, editor. Design and applications of hydroxyapatite-based catalysts. Wiley; 2022. pp. 19-72. DOI
35. Smiciklas, I.; Onjia, A.; Raicević, S.; Janaćković, D.; Mitrić, M. Factors influencing the removal of divalent cations by hydroxyapatite. *J. Hazard. Mater.* **2008**, *152*, 876-84. DOI PubMed
36. Shimabayashi, S.; Tamura, C.; Nakagaki, M. Adsorption of mono- and divalent metal cations on hydroxyapatite in water. *Chem. Pharm. Bull.* **1981**, *29*, 2116-22. DOI

37. Takeuchi, Y.; Arai, H. Removal of coexisting Pb^{2+}, Cu^{2+} and Cd^{2+} ions from water by addition of hydroxyapatite powder. *J. Chem. Eng. Japan.* **1990**, *23*, 75-80. DOI
38. Peng, S.; Lin, Y.; Lee, W.; Lin, Y.; Hung, M.; Lin, K. Removal of Cu^{2+} from wastewater using eco-hydroxyapatite synthesized from marble sludge. *Mater. Chem. Phys.* **2023**, *293*, 126854. DOI
39. Geng, Z.; Cui, Z.; Li, Z.; et al. Synthesis, characterization and the formation mechanism of magnesium- and strontium-substituted hydroxyapatite. *J. Mater. Chem. B.* **2015**, *3*, 3738-46. DOI
40. Saito, T.; Yokoi, T.; Nakamura, A.; Matsunaga, K. Formation energies and site preference of substitutional divalent cations in carbonated apatite. *J. Am. Ceram. Soc.* **2020**, *103*, 5354-64. DOI
41. Oh, S. C.; Lei, Y.; Chen, H.; Liu, D. Catalytic consequences of cation and anion substitutions on rate and mechanism of oxidative coupling of methane over hydroxyapatite catalysts. *Fuel* **2017**, *191*, 472-85. DOI
42. Liu, H.; Cui, X.; Lu, X.; Liu, X.; Zhang, L.; Chan, T. Mechanism of Mn incorporation into hydroxyapatite: Insights from SR-XRD, Raman, XAS, and DFT calculation. *Chem. Geol.* **2021**, *579*, 120354. DOI
43. Ellis, D. E.; Terra, J.; Warschkow, O.; et al. A theoretical and experimental study of lead substitution in calcium hydroxyapatite. *Phys. Chem. Chem. Phys.* **2006**, *8*, 967-76. DOI
44. Kandori, K.; Toshima, S.; Wakamura, M.; Fukusumi, M.; Morisada, Y. Effects of modification of calcium hydroxyapatites by trivalent metal ions on the protein adsorption behavior. *J. Phys. Chem. B.* **2010**, *114*, 2399-404. DOI PubMed
45. Singh, G.; Jolly, S. S.; Singh, R. P. Cerium substituted hydroxyapatite mesoporous nanorods: synthesis and characterization for drug delivery applications. *Mater. Today. Proc.* **2020**, *28*, 1460-6. DOI
46. Ciobanu, G.; Maria, B. A.; Luca, C. New cerium(IV)-substituted hydroxyapatite nanoparticles: preparation and characterization. *Ceram. Int.* **2015**, *41*, 12192-201. DOI
47. Ivanova, T.; Frank-Kamenetskaya, O.; Kol'tsov, A.; Ugolkov, V. Crystal structure of calcium-deficient carbonated hydroxyapatite. thermal decomposition. *J. Solid. State. Chem.* **2001**, *160*, 340-9. DOI
48. Resende, N. S.; Nele, M.; Salim, V. M. Effects of anion substitution on the acid properties of hydroxyapatite. *Thermochim. Acta.* **2006**, *451*, 16-21. DOI
49. Astala, R.; Stott, M. J. First principles investigation of mineral component of bone: CO_3 substitutions in hydroxyapatite. *Chem. Mater.* **2005**, *17*, 4125-33. DOI
50. Lunsford, J. H. The catalytic oxidative coupling of methane. *Angew. Chem. Int. Ed.* **1995**, *34*, 970-80. DOI
51. Arndt, S.; Otremba, T.; Simon, U.; Yildiz, M.; Schubert, H.; Schomäcker, R. Mn-Na_2WO_4/SiO_2 as catalyst for the oxidative coupling of methane. What is really known? *Appl. Catal. A. Gen.* **2012**, *425-6*, 53-61. DOI
52. Feng, R.; Niu, P.; Wang, Q.; et al. In-depth understanding of the crystal-facet effect of $La_2O_2CO_3$ for low-temperature oxidative coupling of methane. *Fuel* **2022**, *308*, 121848. DOI
53. Wang, Z.; Wang, D.; Gong, X. Strategies to improve the activity while maintaining the selectivity of oxidative coupling of methane at La_2O_3: a density functional theory study. *ACS. Catal.* **2020**, *10*, 586-94. DOI
54. Park, J. H.; Lee, D.; Im, S.; et al. Oxidative coupling of methane using non-stoichiometric lead hydroxyapatite catalyst mixtures. *Fuel* **2012**, *94*, 433-9. DOI
55. Lee, K. Y.; Han, Y. C.; Suh, D. J.; Park, T. J. Pb-substituted hydroxyapatite catalysts prepared by coprecipitation method for oxidative coupling of methane. *Stud. Surf. Sci. Catal.* **1998**, *119*, 385-90. DOI
56. Bae, Y. K.; Jun, J. H.; Yoon, K. J. Oxidative coupling of methane over promoted strontium chlorapatite. *Korean. J. Chem. Eng.* **1999**, *16*, 595-601. DOI
57. Sugiyama, S.; Fujii, Y.; Hayashi, H. Oxidative coupling of methane on calcium-lead and barium-lead hydroxyapatites. *Phosphorus. Res. Bull.* **2002**, *14*, 111-8. DOI
58. Oh, S. C.; Wu, Y.; Tran, D. T.; Lee, I. C.; Lei, Y.; Liu, D. Influences of cation and anion substitutions on oxidative coupling of methane over hydroxyapatite catalysts. *Fuel* **2016**, *167*, 208-17. DOI
59. Matsumura, Y.; Sugiyama, S.; Hayashi, H.; Moffat, J. B. Lead-calcium hydroxyapatite: cation effects in the oxidative coupling of methane. *J. Solid. State. Chem.* **1995**, *114*, 138-45. DOI
60. Oh, S. C.; Xu, J.; Tran, D. T.; Liu, B.; Liu, D. Effects of controlled crystalline surface of hydroxyapatite on methane oxidation reactions. *ACS. Catal.* **2018**, *8*, 4493-507. DOI
61. Xiang, D.; Li, P.; Yuan, X. Process optimization, exergy efficiency, and life cycle energy consumption-GHG emissions of the propane-to-propylene with/without hydrogen production process. *J. Clean. Prod.* **2022**, *367*, 133024. DOI
62. Atanga, M. A.; Rezaei, F.; Jawad, A.; Fitch, M.; Rownaghi, A. A. Oxidative dehydrogenation of propane to propylene with carbon dioxide. *Appl. Catal. B. Environ.* **2018**, *220*, 429-45. DOI
63. Carter, J. H.; Bere, T.; Pitchers, J. R.; et al. Direct and oxidative dehydrogenation of propane: from catalyst design to industrial application. *Green. Chem.* **2021**, *23*, 9747-99. DOI
64. Yu, C.; Ge, Q.; Xu, H.; Li, W. Influence of oxygen addition on the reaction of propane catalytic dehydrogenation to propylene over modified Pt-based catalysts. *Ind. Eng. Chem. Res.* **2007**, *46*, 8722-8. DOI
65. Barman, S.; Maity, N.; Bhatte, K.; et al. Single-site VO_x moieties generated on silica by surface organometallic chemistry: a way to enhance the catalytic activity in the oxidative dehydrogenation of propane. *ACS. Catal.* **2016**, *6*, 5908-21. DOI
66. Sugiyama, S.; Shono, T.; Makino, D.; Moriga, T.; Hayashi, H. Enhancement of the catalytic activities in propane oxidation and H-D exchangeability of hydroxyl groups by the incorporation with cobalt into strontium hydroxyapatite. *J. Catal.* **2003**, *214*, 8-14. DOI

67. Boucetta, C.; Kacimi, M.; Ensuque, A.; Piquemal, J.; Bozon-Verduraz, F.; Ziyad, M. Oxidative dehydrogenation of propane over chromium-loaded calcium-hydroxyapatite. *Appl. Catal. A. Gen.* **2009**, *356*, 201-10. DOI
68. Sugiyama, S.; Osaka, T.; Hirata, Y.; Sotowa, K. Enhancement of the activity for oxidative dehydrogenation of propane on calcium hydroxyapatite substituted with vanadate. *Appl. Catal. A. Gen.* **2006**, *312*, 52-8. DOI
69. Petit, S.; Thomas, C.; Millot, Y.; Krafft, J.; Laberty-Robert, C.; Costentin, G. Activation of C-H bond of propane by strong basic sites generated by bulk proton conduction on V-modified hydroxyapatites for the formation of propene. *ChemCatChem* **2020**, *12*, 2506-21. DOI
70. Smith, S. M.; Oopathum, C.; Weeramongkhonlert, V.; et al. Transesterification of soybean oil using bovine bone waste as new catalyst. *Bioresour. Technol.* **2013**, *143*, 686-90. DOI
71. Al-Sakkari, E. G.; Mohammed, M. G.; Elozeiri, A. A.; et al. Comparative technoeconomic analysis of using waste and virgin cooking oils for biodiesel production. *Front. Energy. Res.* **2020**, *8*, 583357. DOI
72. Changmai, B.; Vanlalveni, C.; Ingle, A. P.; Bhagat, R.; Rokhum, S. L. Widely used catalysts in biodiesel production: a review. *RSC. Adv.* **2020**, *10*, 41625-79. DOI PubMed PMC
73. Badnore, A. U.; Jadhav, N. L.; Pinjari, D. V.; Pandit, A. B. Efficacy of newly developed nano-crystalline calcium oxide catalyst for biodiesel production. *Chem. Eng. Process. Process. Intensif.* **2018**, *133*, 312-9. DOI
74. Marinković, D. M.; Stanković, M. V.; Veličković, A. V.; et al. Calcium oxide as a promising heterogeneous catalyst for biodiesel production: current state and perspectives. *Renew. Sustain. Energy. Rev.* **2016**, *56*, 1387-408. DOI
75. Chen, G.; Shan, R.; Shi, J.; Liu, C.; Yan, B. Biodiesel production from palm oil using active and stable K doped hydroxyapatite catalysts. *Energy. Convers. Manag.* **2015**, *98*, 463-9. DOI
76. Chakraborty, R.; Das, S. K. Optimization of biodiesel synthesis from waste frying soybean oil using fish scale-supported Ni catalyst. *Ind. Eng. Chem. Res.* **2012**, *51*, 8404-14. DOI
77. Yan, B.; Zhang, Y.; Chen, G.; Shan, R.; Ma, W.; Liu, C. The utilization of hydroxyapatite-supported CaO-CeO_2 catalyst for biodiesel production. *Energy. Convers. Manag.* **2016**, *130*, 156-64. DOI
78. Ghanei, R.; Khalili Dermani, R.; Salehi, Y.; Mohammadi, M. Waste animal bone as support for CaO impregnation in catalytic biodiesel production from vegetable oil. *Waste. Biomass. Valor.* **2016**, *7*, 527-32. DOI
79. Essamlali, Y.; Amadine, O.; Larzek, M.; Len, C.; Zahouily, M. Sodium modified hydroxyapatite: highly efficient and stable solid-base catalyst for biodiesel production. *Energy. Convers. Manag.* **2017**, *149*, 355-67. DOI
80. Xie, W.; Han, Y.; Tai, S. Biodiesel production using biguanide-functionalized hydroxyapatite-encapsulated-γ-Fe_2O_3 nanoparticles. *Fuel* **2017**, *210*, 83-90. DOI
81. Gupta, J.; Agarwal, M.; Dalai, A. K. Marble slurry derived hydroxyapatite as heterogeneous catalyst for biodiesel production from soybean oil. *Can. J. Chem. Eng.* **2018**, *96*, 1873-80. DOI
82. Khan, H. M.; Iqbal, T.; Ali, C. H.; Yasin, S.; Jamil, F. Waste quail beaks as renewable source for synthesizing novel catalysts for biodiesel production. *Renew. Energy.* **2020**, *154*, 1035-43. DOI
83. Alipour, Z.; Babu Borugadda, V.; Wang, H.; Dalai, A. K. Syngas production through dry reforming: a review on catalysts and their materials, preparation methods and reactor type. *Chem. Eng. J.* **2023**, *452*, 139416. DOI
84. Göransson, K.; Söderlind, U.; He, J.; Zhang, W. Review of syngas production via biomass DFBGs. *Renew. Sustain. Energy. Rev.* **2011**, *15*, 482-92. DOI
85. Fiore, M.; Magi, V.; Viggiano, A. Internal combustion engines powered by syngas: a review. *Appl. Energy.* **2020**, *276*, 115415. DOI
86. Song, Y.; Ozdemir, E.; Ramesh, S.; et al. Dry reforming of methane by stable Ni-Mo nanocatalysts on single-crystalline MgO. *Science* **2020**, *367*, 777-81. DOI
87. Zhou, Q.; Fu, X.; Hui Lim, K.; et al. Complete confinement of Ce/Ni within SiO_2 nanotube with high oxygen vacancy concentration for CO_2 methane reforming. *Fuel* **2022**, *325*, 124819. DOI
88. Tanimu, A.; Yusuf, B. O.; Lateef, S.; et al. Dry reforming of methane: advances in coke mitigation strategies via siliceous catalyst formulations. *J. Environ. Chem. Eng.* **2024**, *12*, 113873. DOI
89. Akri, M.; Zhao, S.; Li, X.; et al. Atomically dispersed nickel as coke-resistant active sites for methane dry reforming. *Nat. Commun.* **2019**, *10*, 5181. DOI PubMed PMC
90. Meng, J.; Pan, W.; Gu, T.; et al. One-pot synthesis of a highly active and stable Ni-embedded hydroxyapatite catalyst for syngas production via dry reforming of methane. *Energy. Fuels.* **2021**, *35*, 19568-80. DOI
91. Rego de Vasconcelos, B.; Pham Minh, D.; Martins, E.; Germeau, A.; Sharrock, P.; Nzihou, A. Highly-efficient hydroxyapatite-supported nickel catalysts for dry reforming of methane. *Int. J. Hydrogen. Energy.* **2020**, *45*, 18502-18. DOI
92. Tran, T. Q.; Pham Minh, D.; Phan, T. S.; Pham, Q. N.; Nguyen Xuan, H. Dry reforming of methane over calcium-deficient hydroxyapatite supported cobalt and nickel catalysts. *Chem. Eng. Sci.* **2020**, *228*, 115975. DOI
93. Boukha, Z.; Kacimi, M.; Pereira, M. F. R.; Faria, J. L.; Figueiredo, J. L.; Ziyad, M. Methane dry reforming on Ni loaded hydroxyapatite and fluoroapatite. *Appl. Catal. A. Gen.* **2007**, *317*, 299-309. DOI
94. Phan, T. S.; Sane, A. R.; Rêgo de Vasconcelos, B.; et al. Hydroxyapatite supported bimetallic cobalt and nickel catalysts for syngas production from dry reforming of methane. *Appl. Catal. B. Environ.* **2018**, *224*, 310-21. DOI
95. Rêgo De Vasconcelos, B.; Zhao, L.; Sharrock, P.; Nzihou, A.; Pham Minh, D. Catalytic transformation of carbon dioxide and methane into syngas over ruthenium and platinum supported hydroxyapatites. *App. Surf. Sci.* **2016**, *390*, 141-56. DOI
96. Akri, M.; El Kasmi, A.; Batiot-Dupeyrat, C.; Qiao, B. Highly active and carbon-resistant nickel single-atom catalysts for methane dry

reforming. *Catalysts* **2020**, *10*, 630. DOI

97. Li, B.; Yuan, X.; Li, B.; Wang, X. Impact of pore structure on hydroxyapatite supported nickel catalysts (Ni/HAP) for dry reforming of methane. *Fuel. Proc. Technol.* **2020**, *202*, 106359. DOI
98. Rego de Vasconcelos, B.; Pham Minh, D.; Sharrock, P.; Nzihou, A. Regeneration study of Ni/hydroxyapatite spent catalyst from dry reforming. *Catal. Today.* **2018**, *310*, 107-15. DOI
99. Dębek, R.; Motak, M.; Duraczyska, D.; et al. Methane dry reforming over hydrotalcite-derived Ni-Mg-Al mixed oxides: the influence of Ni content on catalytic activity, selectivity and stability. *Catal. Sci. Technol.* **2016**, *6*, 6705-15. DOI
100. Parkinson, B.; Matthews, J. W.; Mcconnaughy, T. B.; Upham, D. C.; Mcfarland, E. W. Techno-economic analysis of methane pyrolysis in molten metals: decarbonizing natural gas. *Chem. Eng. Technol.* **2017**, *40*, 1022-30. DOI
101. Elbadawi, A. H.; Ge, L.; Li, Z.; Liu, S.; Wang, S.; Zhu, Z. Catalytic partial oxidation of methane to syngas: review of perovskite catalysts and membrane reactors. *Catal. Rev.* **2021**, *63*, 1-67. DOI
102. Jun, J. Nickel-calcium phosphate/hydroxyapatite catalysts for partial oxidation of methane to syngas: characterization and activation. *J. Catal.* **2004**, *221*, 178-90. DOI
103. Matsumura, Y.; Moffat, J. Partial oxidation of methane to carbon-monoxide and hydrogen with molecular-oxygen and nitrous-oxide over hydroxyapatite catalysts. *J. Catal.* **1994**, *148*, 323-33. DOI
104. Sugiyama, S.; Minami, T.; Higaki, T.; Hayashi, H.; Moffat, J. B. High selective conversion of methane to carbon monoxide and the effects of chlorine additives in the gas and solid phases on the oxidation of methane on strontium hydroxyapatites. *Ind. Eng. Chem. Res.* **1997**, *36*, 328-34. DOI
105. Sugiyama, S.; Abe, K.; Minami, T.; Hayashi, H.; Moffat, J. B. A comparative study of the oxidation of methane and ethane on calcium hydroxyapatites with incorporated lead in the presence and absence of tetrachloromethane. *Appl. Catal. A. Gen.* **1998**, *169*, 77-86. DOI
106. Sugiyama, S.; Fujii, Y.; Abe, K.; Hayashi, H.; Moffat, J. B. Facile formation of the partial oxidation and oxidative-coupling products from the oxidation of methane on barium hydroxyapatites with tetrachloromethane. *Energy. Fuels.* **1999**, *13*, 637-40. DOI
107. Sugiyama, S. Oxidation of methane with nitrous oxide on calcium hydroxyapatites in the presence and absence of tetrachloromethane. *J. Mol. Catal. A. Chem.* **1999**, *144*, 347-55. DOI
108. Jun, J. H.; Lee, S. J.; Lee, S.; et al. Characterization of a nickel-strontium phosphate catalyst for partial oxidation of methane. *Korean. J. Chem. Eng.* **2003**, *20*, 829-34. DOI
109. Jun, J. H.; Jeong, K. S.; Lee, T.; et al. Nickel-calcium phosphate/hydroxyapatite catalysts for partial oxidation of methane to syngas: effect of composition. *Korean. J. Chem. Eng.* **2004**, *21*, 140-6. DOI
110. Kim, K. H.; Lee, S. Y.; Nam, S.; Lim, T. H.; Hong, S.; Yoon, K. J. Promotion effects of ceria in partial oxidation of methane over Ni-calcium hydroxyapatite. *Korean. J. Chem. Eng.* **2006**, *23*, 17-20. DOI
111. Jun, J.; Lim, T.; Nam, S.; Hong, S.; Yoon, K. Mechanism of partial oxidation of methane over a nickel-calcium hydroxyapatite catalyst. *Appl. Catal. A. Gen.* **2006**, *312*, 27-34. DOI
112. Boukha, Z.; Gil-Calvo, M.; de Rivas, B.; González-Velasco, J. R.; Gutiérrez-Ortiz, J. I.; López-Fonseca, R. Behaviour of Rh supported on hydroxyapatite catalysts in partial oxidation and steam reforming of methane: on the role of the speciation of the Rh particles. *Appl. Catal. A. Gen.* **2018**, *556*, 191-203. DOI
113. Ding, K.; Gulec, A.; Johnson, A. M.; et al. Identification of active sites in CO oxidation and water-gas shift over supported Pt catalysts. *Science* **2015**, *350*, 189-92. DOI
114. Haruta, M. Gold catalysts prepared by coprecipitation for low-temperature oxidation of hydrogen and of carbon monoxide. *J. Catal.* **1989**, *115*, 301-9. DOI
115. Green, I. X.; Tang, W.; Neurock, M.; Yates, J. T. J. Spectroscopic observation of dual catalytic sites during oxidation of CO on a Au/TiO_2 catalyst. *Science* **2011**, *333*, 736-9. DOI
116. Guzman, J.; Gates, B. C. Catalysis by supported gold: correlation between catalytic activity for CO oxidation and oxidation states of gold. *J. Am. Chem. Soc.* **2004**, *126*, 2672-3. DOI
117. Zhao, K.; Qiao, B.; Wang, J.; Zhang, Y.; Zhang, T. A highly active and sintering-resistant Au/FeO_x-hydroxyapatite catalyst for CO oxidation. *Chem. Commun.* **2011**, *47*, 1779-81. DOI
118. Huang, J.; Wang, L.; Liu, Y.; Cao, Y.; He, H.; Fan, K. Gold nanoparticles supported on hydroxylapatite as high performance catalysts for low temperature CO oxidation. *Appl. Catal. B. Environ.* **2011**, *101*, 560-9. DOI
119. Domínguez, M. I.; Romero-Sarria, F.; Centeno, M. A.; Odriozola, J. A. Gold/hydroxyapatite catalysts: synthesis, characterization and catalytic activity to CO oxidation. *Appl. Catal. B. Environ.* **2009**, *87*, 245-51. DOI
120. Tang, H.; Wei, J.; Liu, F.; et al. Strong metal-support interactions between gold nanoparticles and nonoxides. *J. Am. Chem. Soc.* **2016**, *138*, 56-9. DOI
121. Zhao, K.; Qiao, B.; Zhang, Y.; Wang, J. The roles of hydroxyapatite and FeO_x in a Au/FeO_x hydroxyapatite catalyst for CO oxidation. *Chin. J. Catal.* **2013**, *34*, 1386-94. DOI
122. Guo, J.; Yu, H.; Dong, F.; Zhu, B.; Huang, W.; Zhang, S. High efficiency and stability of Au-Cu/hydroxyapatite catalyst for the oxidation of carbon monoxide. *RSC. Adv.* **2017**, *7*, 45420-31. DOI
123. Boukha, Z.; Ayastuy, J. L.; Cortés-Reyes, M.; Alemany, L. J.; González-Velasco, J. R.; Gutiérrez-Ortiz, M. A. Catalytic performance of Cu/hydroxyapatite catalysts in CO preferential oxidation in H_2-rich stream. *Int. J. Hydrogen. Energy.* **2019**, *44*, 12649-60. DOI
124. Ratnasamy, C.; Wagner, J. P. Water gas shift catalysis. *Catal. Rev.* **2009**, *51*, 325-440. DOI

125. Zhu, M.; Wachs, I. E. Iron-based catalysts for the high-temperature water-gas shift (HT-WGS) reaction: a review. *ACS. Catal.* **2016**, *6*, 722-32. DOI
126. Miao, D.; Goldbach, A.; Xu, H. Platinum/apatite water-gas shift catalysts. *ACS. Catal.* **2016**, *6*, 775-83. DOI
127. Ding, X.; Liu, W.; Zhao, J.; Wang, L.; Zou, Z. Photothermal CO_2 catalysis toward the synthesis of solar fuel: from material and reactor engineering to techno-economic analysis. *Adv. Mater.* **2025**, *37*, e2312093. DOI
128. Choi, S. H.; Song, I.; Dong, W. J. Recent progress of photothermal catalysts for carbon dioxide conversion. *Energy. Mater.* **2025**, *5*, 500062. DOI
129. Medina, O. E.; Amell, A. A.; López, D.; Santamaría, A. Comprehensive review of nickel-based catalysts advancements for CO_2 methanation. *Renew. Sustain. Energy. Rev.* **2025**, *207*, 114926. DOI
130. Cheng, S.; Sun, Z.; Lim, K. H.; et al. Integrating plasmon and vacancies over oxide perovskite for synergistic CO_2 methanation. *Nano. Energy.* **2025**, *139*, 110917. DOI
131. Medeiros, F. G. M. D.; Ramalho, T. E. B.; Lotfi, S.; Rego de Vasconcelos, B. Direct flue gas hydrogenation to methane over hydroxyapatite-supported nickel catalyst. *Fuel. Proc. Technol.* **2023**, *245*, 107750. DOI
132. Peng, Y.; Szalad, H.; Nikacevic, P.; et al. Co-doped hydroxyapatite as photothermal catalyst for selective CO_2 hydrogenation. *Appl. Catal. B. Environ.* **2023**, *333*, 122790. DOI
133. Guo, J.; Duchesne, P. N.; Wang, L.; et al. High-performance, scalable, and low-cost copper hydroxyapatite for photothermal CO_2 reduction. *ACS. Catal.* **2020**, *10*, 13668-81. DOI
134. Wai, M. H.; Ashok, J.; Dewangan, N.; et al. Influence of surface formate species on methane selectivity for carbon dioxide methanation over nickel hydroxyapatite catalyst. *ChemCatChem* **2020**, *12*, 6410-9. DOI
135. Boukha, Z.; Bermejo-López, A.; Pereda-Ayo, B.; González-Marcos, J. A.; González-Velasco, J. R. Study on the promotional effect of lanthana addition on the performance of hydroxyapatite-supported Ni catalysts for the CO_2 methanation reaction. *Appl. Catal. B. Environ.* **2022**, *314*, 121500. DOI
136. Nguyen, T. T. V.; Phung Anh, N.; Ho, T. G.; et al. Hydroxyapatite derived from salmon bone as green ecoefficient support for ceria-doped nickel catalyst for CO_2 methanation. *ACS. Omega.* **2022**, *7*, 36623-33. DOI PubMed PMC
137. Schiavoni, M.; Campisi, S.; Carniti, P.; Gervasini, A.; Delplanche, T. Focus on the catalytic performances of Cu-functionalized hydroxyapatites in NH_3-SCR reaction. *Appl. Catal. A. Gen.* **2018**, *563*, 43-53. DOI
138. Wang, J.; Liu, J.; Lu, Y.; Hong, D.; Yang, X. Catalytic performance of gold nanoparticles using different crystallinity HAP as carrier materials. *Mater. Res. Bull.* **2014**, *55*, 190-7. DOI
139. Haruta, M.; Kobayashi, T.; Sano, H.; Yamada, N. Novel gold catalysts for the oxidation of carbon monoxide at a temperature far below 0 °C. *Chem. Lett.* **1987**, *16*, 405-8. DOI
140. Haruta, M. Size- and support-dependency in the catalysis of gold. *Catal. Today.* **1997**, *36*, 153-66. DOI
141. Kim, D.; Resasco, J.; Yu, Y.; Asiri, A. M.; Yang, P. Synergistic geometric and electronic effects for electrochemical reduction of carbon dioxide using gold-copper bimetallic nanoparticles. *Nat. Commun.* **2014**, *5*, 4948. DOI PubMed
142. Boukha, Z.; Choya, A.; Cortés-Reyes, M.; et al. Influence of the calcination temperature on the activity of hydroxyapatite-supported palladium catalyst in the methane oxidation reaction. *Appl. Catal. B. Environ.* **2020**, *277*, 119280. DOI
143. Kamieniak, J.; Kelly, P. J.; Doyle, A. M.; Banks, C. E. Influence of the metal/metal oxide redox cycle on the catalytic activity of methane oxidation over Pd and Ni doped hydroxyapatite. *Catal. Commun.* **2018**, *107*, 82-6. DOI
144. Das, S.; Lim, K. H.; Gani, T. Z.; Aksari, S.; Kawi, S. Bi-functional CeO_2 coated NiCo-MgAl core-shell catalyst with high activity and resistance to coke and H_2S poisoning in methane dry reforming. *Appl. Catal. B. Environ.* **2023**, *323*, 122141. DOI
145. Zhang, J.; Li, Y.; Song, H.; et al. Tuning metal-support interactions in nickel-zeolite catalysts leads to enhanced stability during dry reforming of methane. *Nat. Commun.* **2024**, *15*, 8566. DOI PubMed PMC
146. Kamieniak, J.; Kelly, P. J.; Banks, C. E.; Doyle, A. M. Methane emission management in a dual-fuel engine exhaust using Pd and Ni hydroxyapatite catalysts. *Fuel* **2017**, *208*, 314-20. DOI
147. Campisi, S.; Galloni, M. G.; Marchetti, S. G.; Auroux, A.; Postole, G.; Gervasini, A. Functionalized iron hydroxyapatite as eco-friendly catalyst for NH_3-SCR reaction: activity and role of iron speciation on the surface. *ChemCatChem* **2020**, *12*, 1676-90. DOI
148. Mateo, D.; Cerrillo, J. L.; Durini, S.; Gascon, J. Fundamentals and applications of photo-thermal catalysis. *Chem. Soc. Rev.* **2021**, *50*, 2173-210. DOI
149. Guo, J.; Liang, Y.; Song, R.; et al. Construction of new active sites: Cu substitution enabled surface frustrated lewis pairs over calcium hydroxyapatite for CO_2 hydrogenation. *Adv. Sci.* **2021**, *8*, e2101382. DOI PubMed PMC
150. Li, B.; Chen, H.; Yuan, X. Influence of different La_2O_3 loading on hydroxyapatite supported nickel catalysts in the dry reforming of methane. *Fuel* **2024**, *369*, 131687. DOI
151. Xiong, C.; Chen, S.; Yang, P.; Zha, S.; Zhao, Z.; Gong, J. Structure-performance relationships for propane dehydrogenation over aluminum supported vanadium oxide. *ACS. Catal.* **2019**, *9*, 5816-27. DOI
152. Xin, Y.; Shirai, T. Noble-metal-free hydroxyapatite activated by facile mechanochemical treatment towards highly-efficient catalytic oxidation of volatile organic compound. *Sci. Rep.* **2021**, *11*, 7512. DOI PubMed PMC
153. Ye, R.; Ding, J.; Reina, T. R.; et al. Design of catalysts for selective CO_2 hydrogenation. *Nat. Synth.* **2025**, *4*, 288-302. DOI
154. Paris, C.; Karelovic, A.; Manrique, R.; et al. CO_2 hydrogenation to methanol with Ga- and Zn-doped mesoporous Cu/SiO_2 catalysts prepared by the aerosol-assisted sol-gel process. *ChemSusChem* **2020**, *13*, 6409-17. DOI
155. Phan, T. S.; Pham Minh, D. New performing hydroxyapatite-based catalysts in dry-reforming of methane. *Int. J. Hydrogen. Energy.*

2023, *48*, 30770-90. DOI

156. Li, X.; Wang, Y.; Wei, X.; Zhao, Y. Effect of Na promoter on the catalytic performance of Pd-Cu/hydroxyapatite catalyst for room-temperature CO oxidation. *Mol. Catal.* **2020**, *491*, 111002. DOI
157. Martínez-Hernández, H.; Mendoza-Nieto, J. A.; Pfeiffer, H.; Ortiz-Landeros, J.; Téllez-Jurado, L. Development of novel nano-hydroxyapatite doped with silver as effective catalysts for carbon monoxide oxidation. *Chem. Eng. J.* **2020**, *401*, 125992. DOI
158. Maluf, S. S.; Tanabe, E. Y.; Nascente, P. A. P.; Assaf, E. M. Study of water - gas-shift reaction over $La_{(1-y)}Sr_yNi_xCo_{(1-x)}O_3$ perovskite as precursors. *Top. Catal.* **2011**, *54*, 210-8. DOI
159. Rabee, A. I.; Cisneros, S.; Zhao, D.; et al. Uncovering the synergy between gold and sodium on ZrO_2 for boosting the reverse water gas shift reaction: in-situ spectroscopic investigations. *Appl. Catal. B. Environ.* **2024**, *345*, 123685. DOI
160. Rodriguez, J. A.; Grinter, D. C.; Liu, Z.; Palomino, R. M.; Senanayake, S. D. Ceria-based model catalysts: fundamental studies on the importance of the metal-ceria interface in CO oxidation, the water-gas shift, CO_2 hydrogenation, and methane and alcohol reforming. *Chem. Soc. Rev.* **2017**, *46*, 1824-41. DOI
161. Iriarte-Velasco, U.; Ayastuy, J. L.; Boukha, Z.; Bravo, R.; Gutierrez-Ortiz, M. Á. Transition metals supported on bone-derived hydroxyapatite as potential catalysts for the Water-Gas Shift reaction. *Renew. Energy.* **2018**, *115*, 641-8. DOI
162. Su, T.; Gong, B.; Xie, X.; Luo, X.; Qin, Z.; Ji, H. Effect of cobalt on the activity of nickel-based/magnesium-substituted hydroxyapatite catalysts for dry reforming of methane. *Chinese. J. Chem. Eng.* **2024**, *76*, 281-91. DOI
163. Boukha, Z.; Bermejo-López, A.; De-La-Torre, U.; González-Velasco, J. R. Behavior of nickel supported on calcium-enriched hydroxyapatite samples for CCU-methanation and ICCU-methanation processes. *Appl. Catal. B. Environ.* **2023**, *338*, 122989. DOI
164. Pan, Q.; Peng, J.; Sun, T.; Wang, S.; Wang, S. Insight into the reaction route of CO_2 methanation: promotion effect of medium basic sites. *Catal. Commun.* **2014**, *45*, 74-8. DOI
165. Čapek, L.; Hájek, M.; Kutálek, P.; Smoláková, L. Aspects of potassium leaching in the heterogeneously catalyzed transesterification of rapeseed oil. *Fuel* **2014**, *115*, 443-51. DOI
166. Nisar, J.; Razaq, R.; Farooq, M.; et al. Enhanced biodiesel production from Jatropha oil using calcined waste animal bones as catalyst. *Renew. Energy.* **2017**, *101*, 111-9. DOI
167. Liu, C. A.; Cui, Y.; Zhou, Y. The recent progress of single-atom catalysts on amorphous substrates for electrocatalysis. *Energy. Mater.* **2025**, *5*, 500001. DOI
168. Yamaguchi, K.; Mori, K.; Mizugaki, T.; Ebitani, K.; Kaneda, K. Creation of a monomeric Ru species on the surface of hydroxyapatite as an efficient heterogeneous catalyst for aerobic alcohol oxidation. *J. Am. Chem. Soc.* **2000**, *122*, 7144-5. DOI
169. Ogo, S.; Maeda, S.; Sekine, Y. Coke resistance of Sr-hydroxyapatite supported Co catalyst for ethanol steam reforming. *Chem. Lett.* **2017**, *46*, 729-32. DOI
170. Bittencourt, A. F. B.; Moraes, P. I. R.; Da Silva, J. L. F. Mechanistic insights into the direct partial oxidation of methane to methanol catalyzed by single-atom transition metals on hydroxyapatite. *ACS. Omega.* **2025**, *10*, 3868-77. DOI PubMed PMC
171. Tounsi, H.; Djemal, S.; Petitto, C.; Delahay, G. Copper loaded hydroxyapatite catalyst for selective catalytic reduction of nitric oxide with ammonia. *Appl. Catal. B. Environ.* **2011**, *107*, 158-63. DOI
172. Lu, Z.; Cheng, Y.; Ma, D.; et al. Substitution of Fe in hydroxyapatite as an efficient single-atom catalyst for oxygen reduction reaction in biofuel cells: a first-principles study. *Appl. Surf. Sci.* **2021**, *539*, 148233. DOI
173. Wang, J.; Li, W.; Di, A.; et al. Boosting C_{6-12} higher alcohols yield from ethanol upgrading over Ca-deficient mesoporous hydroxyapatite through intermediates enrichment of C_4 aldehyde. *ACS. Catal.* **2025**, *15*, 8599-610. DOI
174. Kamieniak, J.; Doyle, A. M.; Kelly, P. J.; Banks, C. E. Novel synthesis of mesoporous hydroxyapatite using carbon nanorods as a hard-template. *Ceram. Int.* **2017**, *43*, 5412-6. DOI
175. Chingakham, C.; Tiwary, C.; Sajith, V. Waste animal bone as a novel layered heterogeneous catalyst for the transesterification of biodiesel. *Catal. Lett.* **2019**, *149*, 1100-10. DOI
176. Bittencourt, A. F. B.; Valença, G. P.; Da Silva, J. L. F. Elucidating the catalytic valorization of ethanol over hydroxyapatite for sustainable butanol production: a first-principles mechanistic study. *J. Phys. Chem. C.* **2024**, *128*, 14663-73. DOI
177. Wang, J.; Yan, X.; Wang, X.; Yang, M.; Xu, D. Selective activation of methane on hydroxyapatite surfaces: Insights from machine learning and density functional theory. *Nano. Energy.* **2024**, *127*, 109762. DOI
178. Brasil, H.; Bittencourt, A. F.; Yokoo, K. C.; et al. Synthesis modification of hydroxyapatite surface for ethanol conversion: The role of the acidic/basic sites ratio. *J. Catal.* **2021**, *404*, 802-13. DOI
179. Cheng, X.; He, Q.; Li, J.; Huang, Z.; Chi, R. Control of pore size of the bubble-template porous carbonated hydroxyapatite microsphere by adjustable pressure. *Cryst. Growth. Des.* **2009**, *9*, 2770-5. DOI
180. Nowicki, D. A. Utilisation of carbon dioxide in the synthesis of multifunctional AB-type carbonated hydroxyapatite compositions. *J. Solid. State. Chem.* **2024**, *334*, 124678. DOI
181. Ojeda-Niño, O. H.; Blanco, C.; Daza, C. E. High temperature CO_2 capture of hydroxyapatite extracted from tilapia scales. *Univ. Sci.* **2017**, *22*, 215-36. DOI
182. Chen, F. F.; Zhu, Y. J.; Xiong, Z. C.; Sun, T. W. Hydroxyapatite nanowires@metal-organic framework core/shell nanofibers: templated synthesis, peroxidase-like activity, and derived flexible recyclable test paper. *Chemistry* **2017**, *23*, 3328-37. DOI PubMed
183. Sun, T. W.; Yu, W. L.; Zhu, Y. J.; et al. Hydroxyapatite nanowire@magnesium silicate core-shell hierarchical nanocomposite: synthesis and application in bone regeneration. *ACS. Appl. Mater. Interfaces.* **2017**, *9*, 16435-47. DOI
184. Yang, Y. H.; Liu, C. H.; Liang, Y. H.; Lin, F. H.; Wu, K. C. Hollow mesoporous hydroxyapatite nanoparticles (hmHANPs) with

enhanced drug loading and pH-responsive release properties for intracellular drug delivery. *J. Mater. Chem. B.* **2013**, *1*, 2447-50. DOI PubMed

185. Omodolor, I. S.; Otor, H. O.; Andonegui, J. A.; Allen, B. J.; Alba-Rubio, A. C. Dual-function materials for CO_2 capture and conversion: a review. *Ind. Eng. Chem. Res.* **2020**, *59*, 17612-31. DOI
186. Annamalai, L.; Liu, Y.; Deshlahra, P. Selective C-H bond activation via NO_x-mediated generation of strong H-abstractors. *ACS. Catal.* **2019**, *9*, 10324-38. DOI
187. Liang, Y.; Li, Z.; Nourdine, M.; Shahid, S.; Takanabe, K. Methane coupling reaction in an oxy-steam stream through an OH radical pathway by using supported alkali metal catalysts. *ChemCatChem* **2014**, *6*, 1245-51. DOI
188. Tu, S.; Guo, Y.; Zhang, Y.; et al. Piezocatalysis and piezo-photocatalysis: catalysts classification and modification strategy, reaction mechanism, and practical application. *Adv. Funct. Mater.* **2020**, *30*, 2005158. DOI
189. Rodriguez, R.; Rangel, D.; Fonseca, G.; Gonzalez, M.; Vargas, S. Piezoelectric properties of synthetic hydroxyapatite-based organic-inorganic hydrated materials. *Results. Phys.* **2016**, *6*, 925-32. DOI
190. Vasquez-Sancho, F.; Abdollahi, A.; Damjanovic, D.; Catalan, G. Flexoelectricity in bones. *Adv. Mater.* **2018**, *30*, 1705316. DOI
191. Zhou, Y.; Wang, H.; Liu, X.; et al. Direct piezocatalytic conversion of methane into alcohols over hydroxyapatite. *Nano. Energy.* **2021**, *79*, 105449. DOI
192. Xue, M.; Jin, Z.; Yang, B.; Xia, C.; Zhu, G. Boosting higher alcohols selectivity via regulating basicity of Ni/hydroxyapatite in ethanol upgrading. *ACS. Catal.* **2024**, *14*, 12654-63. DOI
193. Medeiros, F. G. M. D.; Farzi, F.; Achouri, I. E.; Lotfi, S.; Rego de Vasconcelos, B. Performance of hydroxyapatite-supported catalysts for methane production via CO_2 hydrogenation on semi-pilot scale. *Waste. Biomass. Valor.* **2023**, *14*, 3429-44. DOI